JCB Journal of Cell Biology

ARTICLE

Cavin4 interacts with Bin1 to promote T-tubule formation and stability in developing skeletal muscle

Harriet P. Lo[1], Ye-Wheen Lim[1*], Zherui Xiong[1*], Nick Martel[1], Charles Ferguson[1], Nicholas Ariotti[1], Jean Giacomotto[3,4], James Rae[1], Matthias Floetenmeyer[2], Shayli Varasteh Moradi[5], Ya Gao[1], Vikas A. Tillu[1], Di Xia[6], Huang Wang[7], Samira Rahnama[5], Susan J. Nixon[1], Michele Bastiani[1], Ryan D. Day[1], Kelly A. Smith[1], Nathan J. Palpant[1], Wayne A. Johnston[5], Kirill Alexandrov[5], Brett M. Collins[1], Thomas E. Hall[1], and Robert G. Parton[1,2]

The cavin proteins are essential for caveola biogenesis and function. Here, we identify a role for the muscle-specific component, Cavin4, in skeletal muscle T-tubule development by analyzing two vertebrate systems, mouse and zebrafish. In both models, Cavin4 localized to T-tubules, and loss of Cavin4 resulted in aberrant T-tubule maturation. In zebrafish, which possess duplicated cavin4 paralogs, Cavin4b was shown to directly interact with the T-tubule–associated BAR domain protein Bin1. Loss of both Cavin4a and Cavin4b caused aberrant accumulation of interconnected caveolae within the T-tubules, a fragmented T-tubule network enriched in Caveolin-3, and an impaired Ca^{2+} response upon mechanical stimulation. We propose a role for Cavin4 in remodeling the T-tubule membrane early in development by recycling caveolar components from the T-tubule to the sarcolemma. This generates a stable T-tubule domain lacking caveolae that is essential for T-tubule function.

Introduction

Caveolae are plasma membrane invaginations that are abundant in many mammalian cells and implicated in a number of fundamental cellular processes, including mechanoprotection and mechanosensation, lipid homeostasis, endocytosis, and regulation of signaling pathways (reviewed in Parton, 2018). The formation of caveolae requires a coordinated assembly involving two essential protein components, the caveolins and cavins. Caveolins were the first structural component of caveolae identified; Caveolin-1 (CAV1) and Caveolin-3 (CAV3) are essential for caveola formation in nonmuscle and muscle cells, respectively (Drab et al., 2001; Fra et al., 1995; Hagiwara et al., 2000; Way and Parton, 1995). More recently, the cavin family of caveolae-associated coat proteins (CAVIN1–CAVIN4) have been described (Bastiani et al., 2009; Hansen et al., 2009; Hill et al., 2008; McMahon et al., 2009). Caveolae-associated protein 1 (CAVIN1; previously known as PTRF) is widely expressed and essential for caveolae formation, acting in concert with CAV1 (in nonmuscle cells) and CAV3 (in muscle cells) to generate caveolae (Hill et al., 2008; Liu et al., 2008). Muscle-specific CAVIN4 (muscle-restricted coiled coil [MURC]) is not required for caveola formation but may play a role in caveolar morphology (Bastiani et al., 2009; Ogata et al., 2014; Ogata et al., 2008).

In skeletal muscle, caveolae can account for as much as 50% of the muscle fiber surface (Lo et al., 2015). Consistent with early electron microscope studies proposing that caveolae function as membrane reservoirs in response to increasing membrane tension (Dulhunty and Franzini-Armstrong, 1975; Lee and Schmid-Schönbein, 1995), evidence for caveolae protecting the cell surface against mechanical damage has now been well documented in skeletal muscle (Lo et al., 2015; Seemann et al., 2017; Sinha et al., 2011), endothelial cells (Cheng et al., 2015), and the zebrafish notochord (Lim et al., 2017). Additional roles for caveolae and caveolar components in skeletal muscle have been derived from studies of the transverse-tubule (T-tubule) system, a crucial feature of the muscle surface comprising an extensive network of tubules that penetrate deep into the muscle interior,

[1]Institute for Molecular Bioscience, The University of Queensland, Brisbane, Queensland, Australia; [2]Centre for Microscopy and Microanalysis, The University of Queensland, Brisbane, Queensland, Australia; [3]Queensland Brain Institute, The University of Queensland, Brisbane, Queensland, Australia; [4]Queensland Centre for Mental Health Research, West Moreton Hospital and Health Service and University of Queensland, Brisbane, Queensland, Australia; [5]CSIRO–Queensland University of Technology Synthetic Biology Alliance, ARC Centre of Excellence in Synthetic Biology, Centre for Agriculture and the Bioeconomy, School of Biology and Environmental Science, Queensland University of Technology, Brisbane, Queensland, Australia; [6]Genome Innovation Hub, The University of Queensland, Brisbane, Queensland, Australia; [7]Translational Research Institute, Mater Research Institute, The University of Queensland, Brisbane, Queensland, Australia.

*Y. Lim and Z. Xiong contributed equally to this paper; Correspondence to Robert G. Parton: r.parton@imb.uq.edu.au; N. Ariotti's present address is Mark Wainwright Analytical Centre, University of New South Wales, Sydney, New South Wales, Australia; R.D. Day's present address is Institute for Marine and Antarctic Studies, University of Tasmania, Hobart, Tasmania, Australia; K.A. Smith's present address is Department of Physiology, The University of Melbourne, Parkville, Victoria, Australia.

allowing the propagation of action potentials to facilitate synchronized calcium release (reviewed in Franzini-Armstrong, 2018). The mature T-system has a unique lipid and protein composition distinct from the sarcolemma; how this is generated and maintained is not yet clear. Early morphological studies showed striking chains of interconnected caveolae in developing embryonic muscle (Ishikawa, 1968); these networks were positive for both the T-tubule marker DHPR and CAV3 (Lee et al., 2002; Parton et al., 1997). Further studies showed similarities between T-tubules and caveolae in their sensitivity to cholesterol manipulation (Carozzi et al., 2000). A loss of CAV3 in mice caused T-tubule abnormalities, although T-tubules still develop (Galbiati et al., 2001). It is also apparent that while embryonic T-tubules possess caveolar morphology and components, mature T-tubules in mammals lose their caveolae as the membrane is remodeled (Parton et al., 1997; Schiaffino et al., 1977). How this is achieved remains unknown.

Muscle-specific CAVIN4 was originally identified as a CAVIN2-interacting protein in cardiomyocytes, where its overexpression led to cardiac defects in mice (Ogata et al., 2008). Mutations in *CAVIN4* have been implicated in dilated cardiomyopathy in humans, and expression of these mutations in rat cardiomyocytes led to reduced RhoA activity, lower mRNA levels of hypertrophy markers, and smaller myocyte size (Rodriguez et al., 2011). However, the presence of these *CAVIN4* variants and others in the Genome Aggregation Database (http://gnomad.broadinstitute.org/), suggest that these mutations should also be considered as potential disease modifiers rather than primary disease-causing mutations (Szabadosova et al., 2018). The functional role of Cavin4 in skeletal muscle has not been studied in detail. In mature mammalian skeletal muscle, CAVIN4 localized to the sarcolemmal membrane (Bastiani et al., 2009). CAVIN4 expression also increased in response to injury-induced muscle regeneration via activation of the extracellular-signal-regulated kinase pathway (Tagawa et al., 2008). A *cavin4b* zebrafish mutant has been described, displaying smaller muscle fibers and impaired swimming ability (Housley et al., 2016). Therefore, current evidence suggests that Cavin4 may be involved in muscle repair and/or maintaining cell volume; however, the precise molecular pathways involved require further investigation.

In this study, we sought to define the function of Cavin4 in vertebrate skeletal muscle. Using both mouse and zebrafish systems, we have uncovered a role for Cavin4 in the development of the specialized surface-connected membrane system in muscle. By taking advantage of the rapid and synchronized development of the T-tubule system in the zebrafish embryo, we show that Cavin4 is required for the structural and functional maturation of the T-tubules. Cavin4 interacts with the T-tubule–associated BAR (Bin/Amphiphysin/Rvs) domain protein Bin1. In the absence of Cavin4, T-tubules fail to lose caveolar components and remodel, and as a result, interconnected caveolae accumulate in the T-tubule. This aberrant structure is associated with fragmentation of the T-tubules and functional defects in calcium ion (Ca^{2+}) release. We conclude that Cavin4 plays a crucial role in removal of caveolae during development, a process required for remodeling of the developing T-tubule membrane and the formation of a stable and functional excitation–contraction system.

Results

Characterization of caveolar protein expression in the mouse and zebrafish

To study the role of Cavin4 in skeletal muscle fibers, we examined the expression profile of cavin4 and other caveolar components in both the mouse and the zebrafish, the latter being a well-characterized model of muscle development and function (Berger and Currie, 2012; Keenan and Currie, 2019). In the adult mouse, caveolar components were expressed in both skeletal muscle and heart tissue, with comparatively strong expression levels of the muscle-specific caveolar components *Cavin4* and *Cav3* (Fig. 1, A and B). In adult zebrafish skeletal muscle, we observed strong expression levels of *cav3*, as well as *cavin4a* and *cavin4b* (the two orthologues of mammalian *Cavin4*), with an overall pattern of caveolar gene expression similar to that of mammalian skeletal and heart muscle (Fig. 1 C). In contrast, there were very low expression levels of *cavin4a* and *cavin4b* in the adult zebrafish heart (Fig. 1 D). Western analysis also demonstrated a lack of Cavin4b in adult zebrafish heart tissue (Fig. S1 A).

Consistent with this, whole-mount in situ hybridization (ISH) in developing zebrafish embryos revealed strong expression of both *cavin4a* and *cavin4b* in the myotome at 24 and 48 h postfertilization (hpf), but no *cavin4* expression in the heart up to 7 d postfertilization (dpf; Fig. 1 E; and Fig. S1, B and C). Intriguingly, the two cavin4 paralogs were expressed at different regions within the myotome; *cavin4a* was expressed throughout the somites, while *cavin4b* was expressed predominantly at the somite boundaries. Therefore, *cavin4a* and *cavin4b* are expressed predominantly in the developing zebrafish myotome in overlapping but distinct expression patterns, and the zebrafish heart shows a strikingly different complement of caveolae proteins similar to nonmuscle tissues.

Cavin4 localizes to the sarcolemma and T-tubules of developing muscle fibers

CAVIN4 localizes to the sarcolemma of mature mouse muscle (Bastiani et al., 2009) and both the sarcolemma and T-tubules in cardiomyocytes from adult mice (Ogata et al., 2014). However, skeletal muscle T-tubules are morphologically distinct from those in cardiac tissue. Unlike cardiac T-tubules, mature skeletal muscle T-tubules lack morphological caveolae (Levin and Page, 1980; Parton et al., 1997). Cardiac T-tubules are also a less specialized plasma membrane domain; they are not only transverse but also have protrusions in many directions and vary in diameter from 20 to 450 nm, compared with skeletal muscle T-tubules, which are much smaller, with a diameter of 20–40 nm (Franzini-Armstrong et al., 1975; Ibrahim et al., 2011; Savio-Galimberti et al., 2008). Therefore, we examined CAVIN4 distribution in developing mouse skeletal muscle. Similar to CAV3 (Parton et al., 1997), CAVIN4 localized to internal structures consistent with T-tubule localization in embryonic skeletal muscle (before birth, 16.5 d postcoitum [dpc]), but 3 d after

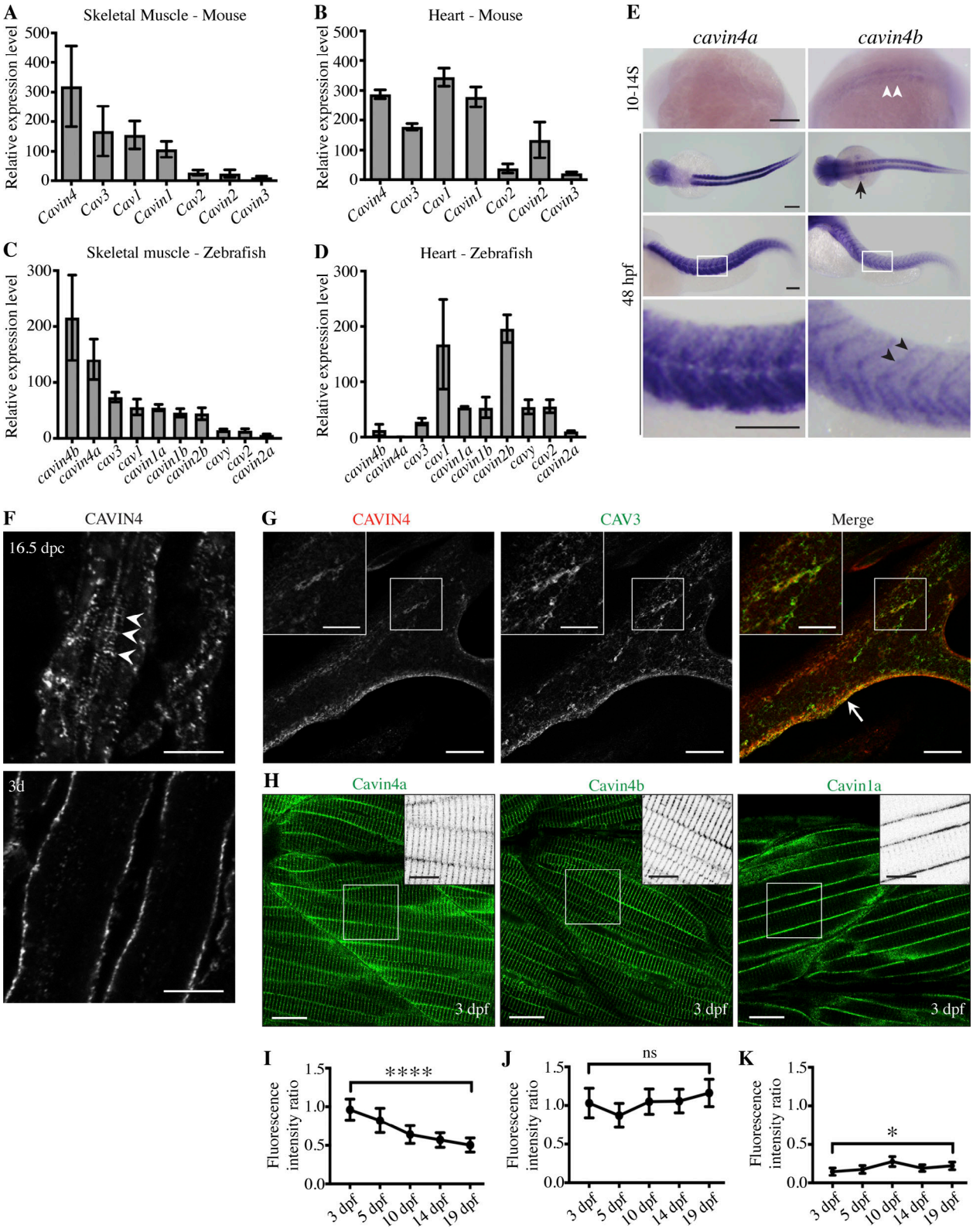

Figure 1. **Cavin4 is associated with T-tubules of developing muscle fibers. (A and B)** qRT-PCR of caveola-associated genes (relative to *36B4*) in 6-mo-old adult WT mouse skeletal muscle (A) and heart tissue (B; mean± SD; *n* = 3 each for muscle and heart). Reactions were performed in the following groups: *Cav1* and *Cavin1*; *Cav2* and *Cav3*; *Cavin2*, *Cavin3*, and *Cavin4*. **(C and D)** qRT-PCR of caveola-associated genes (relative to *β-actin*) in 10-mo-old WT adult zebrafish trunk muscle (C) and heart (D; *n* = 3 for trunk muscle, *n* = 3 pooled samples for heart tissue). For A–D, muscle genes are shown in order of decreasing expression; heart genes are shown in the same order as for muscle samples. **(E)** Whole-mount ISH for *cavin4a* and *cavin4b* in 10- to 14-somite (S) and 48-hpf WT zebrafish embryos. *Cavin4b* expression in adaxial cells (white arrowheads), pectoral fin buds (arrow), and somite boundaries (black arrowheads) is highlighted. Images for 48 hpf shown anterior to left in both dorsal and lateral view; bottom panel shows a magnification of boxed areas. Scale bars: 200 µm. **(F)** Confocal

images of CAVIN4 in mouse skeletal muscle before birth (16.5 dpc) and 3 d after birth (3d). Arrowheads indicate internal labeling. Scale bars: 10 µm. **(G)** Confocal images of CAVIN4 and CAV3 in C2C12 myotubes (arrow, sarcolemmal staining). Insets show a magnification of boxed area. Scale bars: 20 µm (inset, 10 µm). **(H)** Clover-tagged Cavin4a, Cavin4b, and Cavin1a in muscle fibers of 3-dpf transgenic zebrafish embryos. Inverted images = magnification of boxed area. Scale bars: 20 µm (inset, 10 µm). **(I–K)** Ratio of T-tubule to sarcolemmal fluorescence intensity for Cavin4a (I), Cavin4b (J), and Cavin1a (K). $n = 9$ muscle fibers from three embryos per line for each developmental stage (one-way ANOVA with multiple-comparison Tukey's test). ****, $P \leq 0.0001$; *, $P \leq 0.05$. Error bars represent mean ± SD.

birth, CAVIN4 was predominantly localized to the sarcolemmal membrane, with little internal staining (Fig. 1 F). We also examined CAVIN4 localization in the well-characterized C2C12 skeletal muscle cell line. In differentiated C2C12 myotubes, CAVIN4 localized to both the sarcolemma and internal networks, overlapping with CAV3 immunolabeling, consistent with an association with developing T-tubules (Fig. 1 G).

We next analyzed the localization of Cavin4a and Cavin4b in more detail using existing transgenic zebrafish lines expressing Clover-tagged forms of these proteins (Xiong et al., 2021). In developing muscle fibers, both Cavin4a and Cavin4b showed strong localization to the sarcolemma and T-tubules (Fig. 1 H). Quantitation of the ratio of T-tubule to sarcolemmal fluorescence intensity revealed that the levels of Cavin4a-Clover associated with the T-tubules decreased significantly over time, while Cavin4b-Clover maintained a consistent level of T-tubule association over the same developmental period (3–19 dpf; Fig. 1, I–K; and Fig. S1 D). In comparison, Cavin1a (the muscle-specific orthologue of CAVIN1; Lo et al., 2015) was expressed predominantly at the sarcolemma, with only low levels observed in the T-tubule system, and the ratio of T-tubule to sarcolemmal intensity for Cavin1a-Clover was relatively unchanged over the same time period. These observations strongly suggest a specific role for Cavin4, possibly independent of caveolae, in the developing T-tubule system.

CAVIN4-deficient mouse skeletal muscle exhibits ultrastructural defects and abnormal distribution of CAV3

To investigate the effect of a loss of CAVIN4 in skeletal muscle, we first performed a knockout (KO) of *Cavin4* in mouse embryos using a CRISPR-Cas9–based approach. Three single guide RNAs (sgRNAs) were designed for targeted deletion of exon 1 of *Cavin4*; synthesized sgRNAs and Cas9 protein were mixed as ribonucleoproteins and microinjected into zygotes, and embryos were transferred into pseudopregnant female mice. Skeletal muscle was collected from pups 3 d after birth, when CAV3 is predominantly associated the sarcolemma (Parton et al., 1997). PCR-based genotyping analysis identified 5 of 20 pups as likely to harbor homozygous deletions of *Cavin4*; immunostaining of hindlimb muscle revealed a loss of CAVIN4 in these 5 pups (Fig. S1 E). Additional Western and quantitative real-time PCR (qRT-PCR) analysis revealed no detectable levels of Cavin4 in *Cavin4*$^{-/-}$ muscle, demonstrating the efficacy of this approach for generating KO tissue in the F0 generation (Fig. S1, F and G). Interestingly, expression analysis of the classical T-tubule marker *Bin1* (Butler et al., 1997) showed a trend toward up-regulation in *Cavin4*$^{-/-}$ tissue (Fig. S1 G).

Muscle tissue from two *Cavin4*$^{-/-}$ mice were used for further analysis. Immunostaining revealed that a loss of CAVIN4 was associated with increased internal labeling for CAV3; the ratio of fluorescence intensity of sarcolemma to internal labeling was significantly reduced in *Cavin4*$^{-/-}$ muscle fibers, consistent with a higher level of internal labeling (Fig. 2, A and B). Electron microscopic comparison further revealed increased accumulation of tubular membranous elements between myofibers in the absence of CAVIN4 (Fig. 2, C–F). Sparse tubular and vesicular elements between myofibers could be observed in WT muscle. In contrast, *Cavin4*$^{-/-}$ muscle had numerous long tubular elements, including stacked arrays of tubular structures, between the myofibers that were rarely seen in control muscle. Stereological analysis on random sections of WT and *Cavin4*$^{-/-}$ muscle revealed a twofold increase in the volume of the interfiber membrane system (from 3.82% of the cytoplasmic volume to 8.73%; Fig. 2 G).

In parallel, we also created a *Cavin4*$^{-/-}$ C2C12 cell line using CRISPR-Cas9 technology. A single clonal line was identified harboring a homozygous deletion; Western and qRT-PCR analysis confirmed the absence of Cavin4 in this cell line (Fig. S1, I and J). Similar to that observed in muscle tissue, CAV3 immunostaining revealed more internal aggregates and a less extensive internal network in the absence of CAVIN4 (Fig. S1 H). We also noted a significant up-regulation of *Bin1* expression in Cavin4$^{-/-}$ cells (Fig. S1 J).

Taken together, these observations suggested that redistribution of CAV3 from the developing T-tubules to the sarcolemma, a process that occurs from 15 dpc until a few days after birth in the mouse embryo (Parton et al., 1997), was perturbed in the absence of CAVIN4.

Complete loss of Cavin4 in zebrafish embryos causes significant structural T-tubule abnormalities and functional defects

To date, detailed analyses of T-tubule development have been difficult in mammalian systems due to a slow and asynchronous process of T-tubule development. We have recently characterized this process extensively in the developing zebrafish embryo using light microscopy, 3D EM, and semiautomated quantitative assays of T-tubule development (Hall et al., 2020); this system overcomes many of the challenges of the mammalian system and is amenable to precise mechanistic dissection. We therefore generated *cavin4a* and *cavin4b* KO zebrafish lines and crossed them to obtain a zebrafish line completely lacking Cavin4 (*cavin4a;cavin4b* double mutant, hereafter referred to as *cavin4*$^{-/-}$; see Figs. S2 and S3 and Materials and methods for a detailed description of the generation and characterization of individual *cavin4a*$^{-/-}$ and *cavin4b*$^{-/-}$ lines).

Cavin4$^{-/-}$ embryos were viable and morphologically similar to WT embryos (Fig. S4 A). However, while we were able to

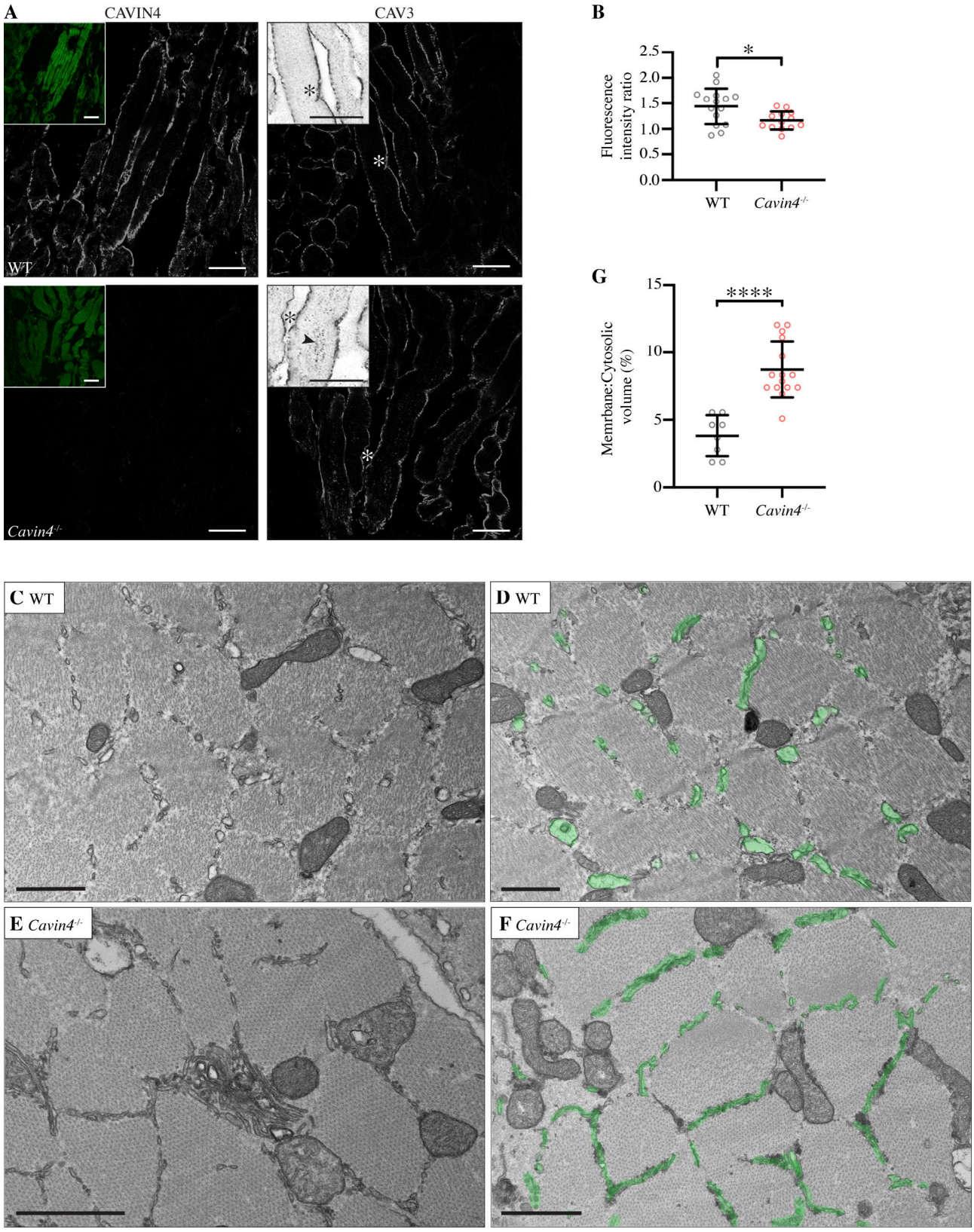

Figure 2. **Loss of CAVIN4 in mouse skeletal muscle causes ultrastructural defects and abnormal distribution of CAV3. (A)** Confocal images of CAVIN4 (with Phalloidin-Alexa488 counterstain, inset) and CAV3 in WT and *Cavin4*$^{-/-}$ 3-d-old mouse skeletal hindlimb muscle. Inverted images show the magnified area highlighted by an asterisk. Arrowhead highlights internal CAV3 labeling. Scale bars: 20 µm. **(B)** Ratio of sarcolemmal to internal CAV3 fluorescence intensity in WT and *Cavin4*$^{-/-}$ skeletal hindlimb muscle (n = 2 each of WT and *Cavin4*$^{-/-}$ samples, two-tailed t test). Quantitation was performed in coded (blinded) samples; colored circles represent measurements from individual images. *, P ≤ 0.05. **(C–F)** EM of hindlimb skeletal muscle from 3-d-old WT and *Cavin4*$^{-/-}$ pups. In WT

muscle (C and D), sparse vesicular elements were visible between the myofibers, generally as vesicular or short tubular structures. *Cavin4*$^{-/-}$ muscle (E and F) exhibited numerous long tubular elements between the myofibers, often forming complex stacked arrays (E) not seen in WT muscle. Tubular structures highlighted in green in D and F. Scale bars: 1 µm. **(G)** Membrane/cytosolic volume (%) in WT and *Cavin4*$^{-/-}$ muscle (n = 2 each of WT and *Cavin4*$^{-/-}$ samples, two-tailed t test). Colored circles represent separate images. ****, P ≤ 0.0001. Error bars represent mean ± SD.

generate adult *cavin4*$^{-/-}$ zebrafish, they were poor breeders, hampering the generation of homozygous clutches; experiments were therefore performed using homozygous × heterozygous crosses, with pre- or postgenotyping to identify *cavin4*$^{-/-}$ embryos. To visualize muscle fibers, we crossed the *cavin4*$^{-/-}$ line to an existing transgenic line expressing ubiquitous GFP-CaaX, which effectively delineates the sarcolemma and T-tubules (Hall et al., 2020; Williams et al., 2011). Imaging of transverse sections from 5-dpf WT embryos revealed GFP localization at the sarcolemma and T-tubules in a characteristic radial "spoke-like" pattern (Fig. 3 A). In *cavin4*$^{-/-}$ embryos, however, we observed striking abnormalities within the T-tubules of some muscle fibers, where the radial T-tubule pattern was fragmented and aggregates were observed instead (Figs. 3 A and S4 B). These T-tubule abnormalities persisted to 10 dpf (Fig. S4 C) but were not present in juvenile *cavin4*$^{-/-}$ zebrafish; normal T-tubule structures were observed at 30 dpf, albeit with more longitudinally oriented tubules (Fig. S4 D).

In view of the effect on the T-tubule system in *Cavin4*$^{-/-}$ mouse skeletal muscle, we next examined the distribution of Cav3. In zebrafish embryos, T-tubules penetrate from the sarcolemma to the fiber midline by 48 hpf (Hall et al., 2020). Imaging of an existing transgenic line expressing Cav3-GFP revealed that Cav3 was strongly associated with early T-tubules during zebrafish development (31 hpf; Fig. 3 B). By 72 hpf, this association with the T-tubules was significantly decreased and Cav3-GFP was predominantly associated with the sarcolemma (Fig. 3, B and C), similar to that observed in mammalian muscle (Parton et al., 1997). We crossed our *cavin4*$^{-/-}$ and Cav3-GFP lines; live imaging revealed T-system aberrations (see longitudinal intensity profiles, Fig. 3 D) and a significantly higher proportion of Cav3-GFP associated with T-tubules in *Cavin4*$^{-/-}$ muscle (Fig. 3 E). A similar redistribution to the T-tubules was observed in the absence of Cavin4a or Cavin4b, suggesting similar but independent roles of the two cavin4 paralogs (Fig. S2, F–K).

We next performed detailed ultrastructural analyses of WT and *cavin4*$^{-/-}$ muscle fibers. An ∼60% reduction in relative caveola density and dramatically reduced density of surface-connected T-tubules was observed in the absence of Cavin4 (Fig. 4, A–C; and Fig. S5, A and B). These aberrations were further investigated using serial blockface scanning EM followed by automated thresholding to reveal the 3D organization in the context of the whole muscle fiber. In WT muscle, 3D reconstruction highlighted the organized T-tubule structure throughout the muscle fiber and connecting to the muscle fiber surface (Fig. 4, D–G). In *cavin4*$^{-/-}$ muscle, however, there was a dramatic loss of T-tubule organization, with few connections to the sarcolemmal surface (Fig. 4, H–K). We further assessed the fine structure of the remnant T-tubules both in thin sections and by using high-resolution electron tomography with 300-nm sections of zebrafish embryonic muscle. These techniques revealed that the remaining T-tubules in *cavin4*$^{-/-}$ muscle fibers had a striking bead-like morphology; 3D reconstruction of these T-tubules showed that they resembled interconnected caveolae (Fig. 4, L–N; and Video 1). In view of this striking similarity between the T-tubule morphology and the chains of caveolae observed in developing muscle (Ishikawa, 1968; Parton et al., 1997) and the increased Cav3 in T-tubules of Cavin4$^{-/-}$ muscle (Fig. 3, D and E), our results suggest that loss of Cavin4 leads to increased accumulation and/or decreased removal of caveolae from the T-tubule system. Overall, the ultrastructural observations highlight a decrease in sarcolemmal caveolae but an increase in caveola-like structures in the dysmorphic T-tubules of Cavin4-null muscle.

In view of the structural defects observed, we investigated whether the function of the T-tubule system in excitation–contraction coupling (Flucher, 1992) was perturbed in the absence of Cavin4. The *cavin4*$^{-/-}$ line was crossed into a stable transgenic line expressing the genetically encoded fluorescent Ca^{2+} indicator GCaMP. Muscle contraction was induced in zebrafish embryos using electrical stimulation, which caused a sharp increase in GCaMP fluorescence intensity, followed by a decrease in intensity in the absence of stimulation (Fig. 4 O). We analyzed two aspects of the Ca^{2+} response in our WT and *cavin4*$^{-/-}$ embryos: (1) decay of response, defined as the time in which the intensity of GFP dropped to 50% of the maximal intensity; and (2) amplitude, calculated as the ratio of fluorescence intensity above the minimum signal in the absence of stimulation. Decay did not appear to be affected in *cavin4*$^{-/-}$ muscle fibers (Fig. 4 P). However, fluorescence amplitude was significantly reduced in *cavin4*$^{-/-}$ embryos in comparison to WT (Fig. 4 Q).

In conclusion, a loss of Cavin4 in the zebrafish is associated with aberrant T-tubule morphology and a significantly reduced Ca^{2+} response upon muscle contraction.

A direct functional interaction between Cavin4 and Bin1 in T-tubule development

Finally, we examined the molecular mechanisms underlying a loss of Cavin4. We recently identified Bin1b/Amphiphysin-2, the muscle-specific BIN1 orthologue in zebrafish (Smith et al., 2014), as a potential interactor of Cavin4b using proximity-dependent biotin labeling and mass spectrometry (Xiong et al., 2021). BIN1 is a major driver of T-tubule formation and has been closely linked to CAV3 in mammalian T-tubule development (Lee et al., 2002). In view of these findings and the observed up-regulation of *BIN1* expression in the absence of CAVIN4 (Figs. S1 G and S1 J), we hypothesized that a functional interaction exists between Cavin4 and Bin1 during T-tubule development.

We first used a model cellular system, as done previously (Hall et al., 2020; Lee et al., 2002), to examine the possible

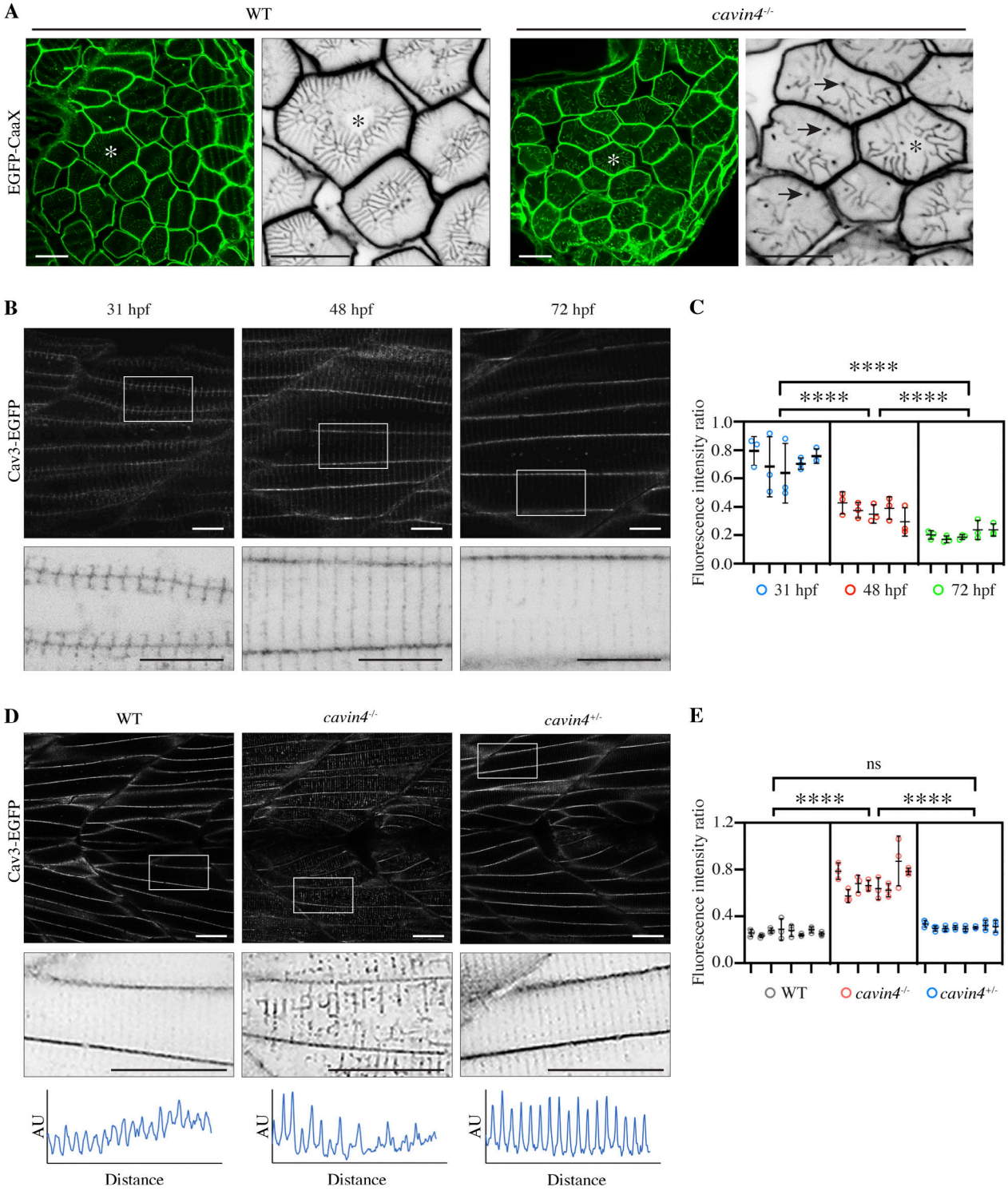

Figure 3. ***Cavin4*$^{-/-}$ zebrafish embryos have an aberrant T-system and increased association of Cav3 with T-tubules. (A)** Confocal images of EGFP-CaaX in transverse sections of WT and *cavin4*$^{-/-}$ 5-dpf embryos. Asterisk indicates corresponding muscle fiber in magnified inverted image. Arrows indicate abnormal puncta in *cavin4*$^{-/-}$ muscle. Scale bars: 10 µm. **(B)** Confocal images of Cav3-EGFP in live zebrafish embryos at 31, 48, and 72 hpf. Inverted images in bottom panel show boxed areas. Scale bars: 10 µm. **(C)** Ratio of T-tubule to sarcolemma fluorescence intensity (n = 5 embryos for each time point in B, n = 3 areas per embryo represented as colored circles; nested one-way ANOVA with multiple-comparison Tukey's test). ****, P ≤ 0.0001. **(D)** Confocal images of Cav3-EGFP in live 5-dpf WT, *cavin4*$^{-/-}$, and *cavin4*$^{+/-}$ (sibling) embryos. Inverted images show magnification of boxed areas. Box scan quantitation of boxed area (bottom panel; AU, arbitrary units) highlights loss of T-tubule periodicity in *cavin4*$^{-/-}$ muscle. Scale bars: 10 µm. **(E)** Ratio of T-tubule to sarcolemma fluorescence intensity in WT, *cavin4*$^{-/-}$, and *cavin4*$^{+/-}$ muscle fibers (n = 8 embryos per genotype from two independent clutches, n = 3 areas per embryo represented as colored circles; nested one-way ANOVA with multiple-comparison Tukey's test). ****, P ≤ 0.0001. Error bars represent mean ± SD.

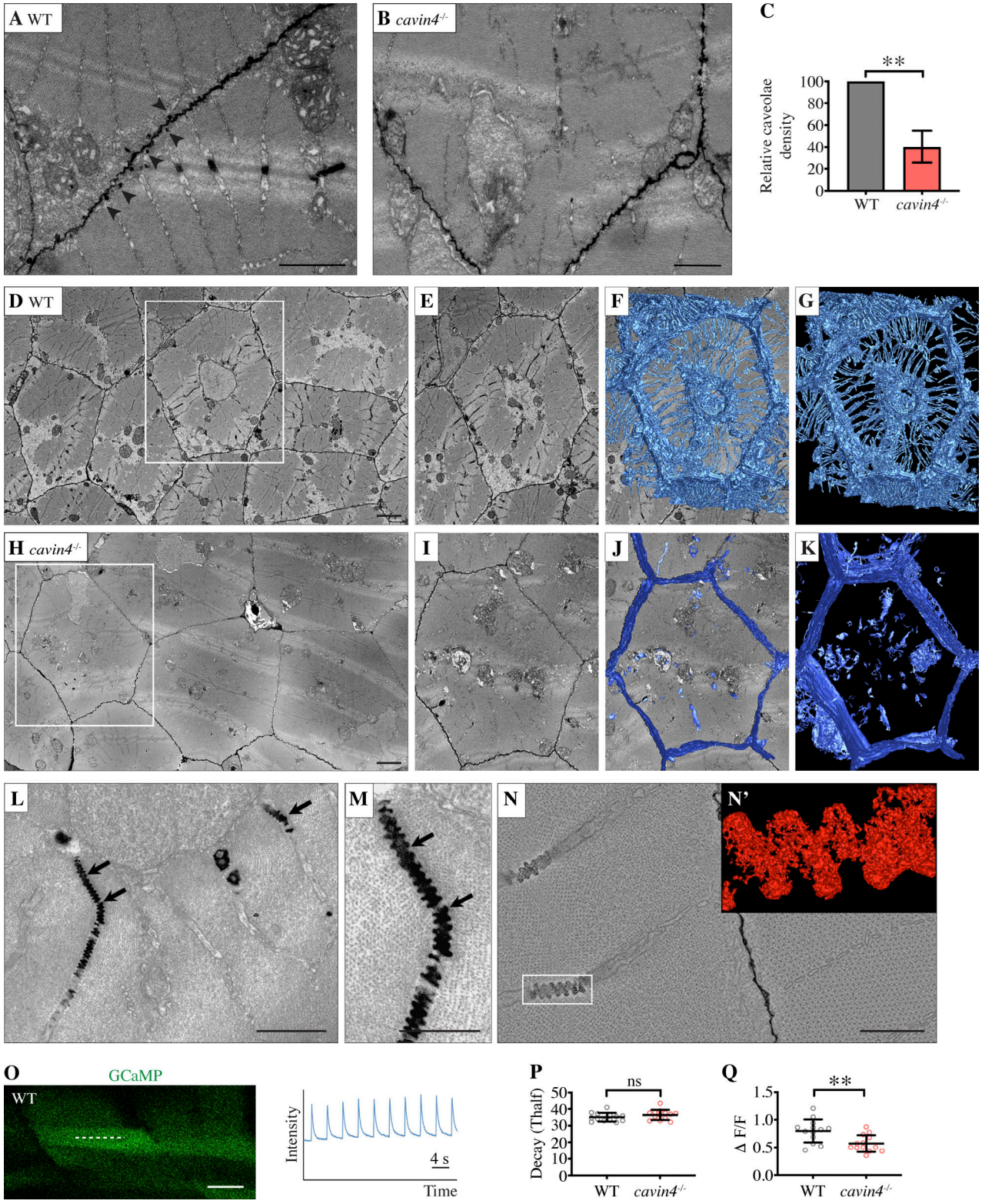

Figure 4. **EM reveals T-tubule irregularities in *cavin4*$^{-/-}$ zebrafish muscle, which are associated with a reduced Ca^{2+} response to muscle contraction.** **(A and B)** Ultrastructure of 5-dpf WT (A) and *cavin4*$^{-/-}$ (B) embryos. Normal sarcomeric T-system structure was observed in WT muscle; arrowheads highlight abundant caveolae. Few caveolae were observed in *cavin4*$^{-/-}$ muscle. Scale bars: 1 µm. **(C)** Relative caveolae density was 40.3 ± 14.7% in muscle from 5-dpf *cavin4*$^{-/-}$ embryos (compared with WT; two-tailed *t* test). **, P ≤ 0.01. Quantitation performed on randomly selected images from three embryos from three different clutches. **(D–K)** Single sections showing skeletal muscle ultrastructure from a 5-dpf WT (D) and *cavin4*$^{-/-}$ zebrafish embryo (H). A single muscle fiber from each WT and *cavin4*$^{-/-}$ section was chosen (E and I, boxed areas in D and H, respectively), and density-based thresholding was used to segment T-tubules. 3D reconstruction highlights normal radial distribution of T-tubules in WT muscle (F and G) and abnormal T-tubule morphology in *cavin4*$^{-/-}$ muscle (J and K). Scale bars: 2 µm. **(L and M)** Remaining T-tubules in *cavin4*$^{-/-}$ muscle fibers had caveolar structure (arrows). Scale bars: 1 µm. **(N)** 3D reconstruction of T-tubule

area from *cavin4*$^{-/-}$ muscle. Inset (N') represents boxed area. Scale bar: 500 nm. See also Video 1. **(O)** Confocal image of GCaMP expression in WT zebrafish muscle, with line scan measurement (dashed line) of GCaMP intensity in response to electrical stimulation (GFP intensity [y axis] over time [seconds, x axis]). Scale bar: 20 µm. **(P and Q)** Quantitation of GCaMP signal in response to electrical stimulation measured as half-life (Thalf) decay (P) and amplitude (Q, ΔF/F) in WT and *cavin4*$^{-/-}$ muscle fibers (two-tailed *t* test). **, P ≤ 0.01. Values for individual embryos shown as colored circles (*n* = 6, 5, and 2 each of WT and *cavin4*$^{-/-}$ embryos from three independent clutches, with an average of at least three fiber measurements per embryo). Error bars represent mean ± SD.

association of Cavin4 with Bin1-induced tubules in nonmuscle cells. Coexpression of Bin1b and Cavin4b produced numerous membrane tubular structures in baby hamster kidney (BHK) cells that were positive for both Bin1b and Cavin4b (Fig. 5 A). In contrast, Cavin4b was not recruited to tubules generated by the expression of the mCherry reporter or the early endosomal marker SNX8, highlighting the specificity of the interaction (Fig. S5, C and D). Coexpression of the mammalian orthologues (CAVIN4 and BIN1) revealed CAVIN4 was associated with BIN1-positive tubules (Fig. 5 B) in a punctate localization pattern similar to that observed for CAV3 and BIN1 (Lee et al., 2002).

We next used this system to examine whether expression of Cavin4 affected Bin1-dependent tubule formation. Live-cell imaging revealed that the formation of Bin1b-positive tubules in BHK cells was dynamic and transient. Quantitation of these tubules showed that both the number of tubules and the size of tubules (tubule area and Feret's diameter) were significantly increased in the presence of Cavin4b (Fig. 5, E and F; and Fig. S5, E and F). These results suggest that Cavin4b enhances the formation of Bin1b-induced membrane tubules, implying a potential role for Cavin4 in promoting T-tubule formation.

To gain further insights into the possible mechanisms involved in Cavin4 recruitment to T-tubules, we examined whether there was a direct interaction between Cavin4b and Bin1b. The two proteins were coexpressed as fusions with mCherry and EGFP in a *Leishmania tarentolae*–based cell-free system and their interaction assessed using Amplified Luminescence Proximity Homogeneous Assay (AlphaLISA) technology. Pairwise assessment of Cavin4a, Cavin4b, Bin1a, and Bin1b indicated a strong interaction between Cavin4b and Bin1b (Fig. 6 A). Consistent with this, Cavin4b-mCherry was also immunoprecipitated from BHK cells coexpressing Bin1b-EGFP (Figs. 6 B and S5 G).

All Bin1 isoforms possess a Src homology 3 (SH3) domain that interacts with proteins containing a proline-rich domain (PRD; Hohendahl et al., 2016; Prokic et al., 2014). Notably, Cavin4b has a putative Bin1-binding PRD between residues 271 to 286 within the disordered region 3 (DR3) domain (Fig. S5 H). Therefore, we hypothesized that there could be an interaction between the Cavin4b PRD and the Bin1b-SH3 domain. Isothermal titration calorimetry (ITC) showed a significant interaction between the Cavin4b PRD peptide and Bin1b-SH3 domain (dissociation constant [K_d] 61.7 ± 2.8 µM; Fig. 6 C). Full-length (FL) Cavin4b and Bin1b-SH3 showed an interaction with a similar affinity (K_d 55.9 ± 2.4 µM), suggesting that no other major SH3-binding domain exists outside of the PRD motif. A peptide from the Chikungunya virus (CHIKV; Fig. S5 H) harbors a proline-rich motif and has a remarkable affinity for the human BIN1-SH3 domain (Tossavainen et al., 2016). We also confirmed a conserved high affinity between the CHIKV peptide and the Bin1b-SH3 domain using ITC (K_d 88.9 ± 2.85 nM; Fig. S5 I), similar to its interaction with human BIN1-SH3 (Tossavainen et al., 2016). To confirm the Cavin4b PRD binds to Bin1b-SH3 in the canonical binding site, we performed a competitive binding assay using the high-affinity CHIKV peptide. As expected, Cavin4b PRD binding was blocked by the competing CHIKV peptide (Fig. 6 C). Cavin4a, which does not possess the PRD in its DR3, did not show any binding affinity toward Bin1b-SH3 (Fig. 6 C). In addition, mutation of the PRD of Cavin4b (P274A/P276T) abolished its localization to Bin1b-positive tubules (Fig. 5 C), demonstrating that this domain is required for Cavin4 recruitment to model T-tubules in this system. Zebrafish Cavin4a, which lacks a similar PRD, was not recruited to Bin1b-positive tubules (Fig. 5 D).

Interaction of proteins with the Bin1-SH3 domain via PRDs has been shown to promote Bin1-driven tubulation (Wu and Baumgart, 2014), consistent with the effect of Cavin4 expression on T-tubule formation. We next hypothesized that high expression of Bin1 might rescue a loss of Cavin4 in vivo. To test this, we injected a DNA construct encoding mKate2-tagged Bin1b into zebrafish embryos at the one-cell stage. This transient mosaic expression of Bin1b allowed us to compare expressing and nonexpressing muscle fibers. Bin1b localized to the sarcolemma and T-tubules of skeletal muscle fibers in transverse sections from WT embryos, overlapping with GFP-CaaX expression (Figs. 6 D and S4 E). Strikingly, *cavin4*$^{-/-}$ muscle fibers expressing Bin1b showed normal T-tubule structure (based on GFP-CaaX expression pattern), revealing that high expression of Bin1b rescued the T-tubule defects caused by lack of Cavin4. Live imaging in longitudinal muscle fibers also showed restored distribution of Cav3-GFP to the sarcolemmal membrane in *cavin4*$^{-/-}$ embryos (Fig. 6, E and F).

In conclusion, these results suggest an interplay between Bin1 and Cavin4 in T-tubule formation and stability. Cavin4b binds directly to zebrafish Bin1b to be recruited to the developing T-tubule system and may help promote Bin1-induced tubulation. Loss of Cavin4 disrupts T-tubule structure and function but can be rescued by high Bin1 expression.

Discussion

In this study, we used a number of complementary approaches to investigate the role of Cavin4 in skeletal muscle. Taking advantage of the zebrafish as a highly tractable model system and our recently developed methods (Hall et al., 2020), we demonstrate that Cavin4 is a direct interactor of Bin1 and plays a crucial role in the remodeling of the T-tubule system during muscle development.

A role for Cavin4 in T-tubule membrane remodeling during development

Our study revealed that the overall profile of *cavin* and *caveolin* expression in zebrafish muscle was comparable to mouse

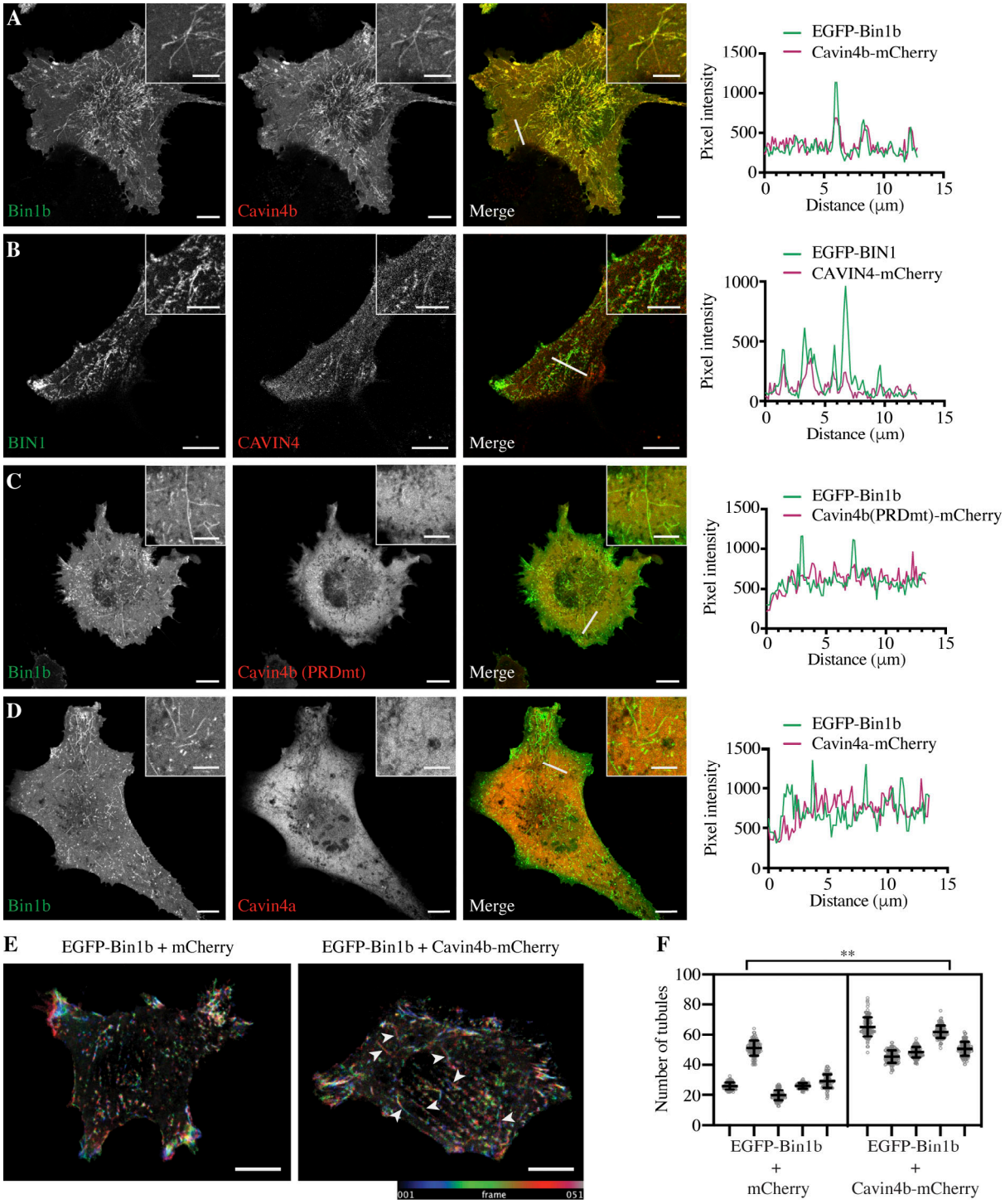

Figure 5. **Cavin4b is recruited to Bin1b-positive tubules in BHK cells. (A–D)** Live confocal imaging of BHK cells cotransfected with: EGFP-Bin1b/Cavin4b-mCherry (A), EGFP-BIN1/CAVIN4-mCherry (B), EGFP-Bin1b/Cavin4b(PRDmt)-mCherry (C), or EGFP-Bin1b/Cavin4a-mCherry (D). Colocalization was analyzed by line scan (as indicated, inset = line scan area) showing pixel intensity over the line distance (far right panel). Images representative of $n = 6$ cells/group and three replicates. Scale bars: 10 µm (insets, 5 µm). **(E)** Time-lapse confocal imaging of BHK cells cotransfected with EGFP-Bin1b/mCherry or EGFP-Bin1b/Cavin4b-mCherry. Each frame was color coded and superimposed into a single image. Arrowheads indicate dynamic Bin1 tubules captured during time lapse. Scale bars: 10 µm. **(F)** Scatter plot quantitation of number of Bin1b-positive tubules (normalized to cell size) captured during live cell imaging (6 min; $n = 5$ cells; nested two-tailed t test). **, $P \leq 0.01$. Error bars represent mean ± SD.

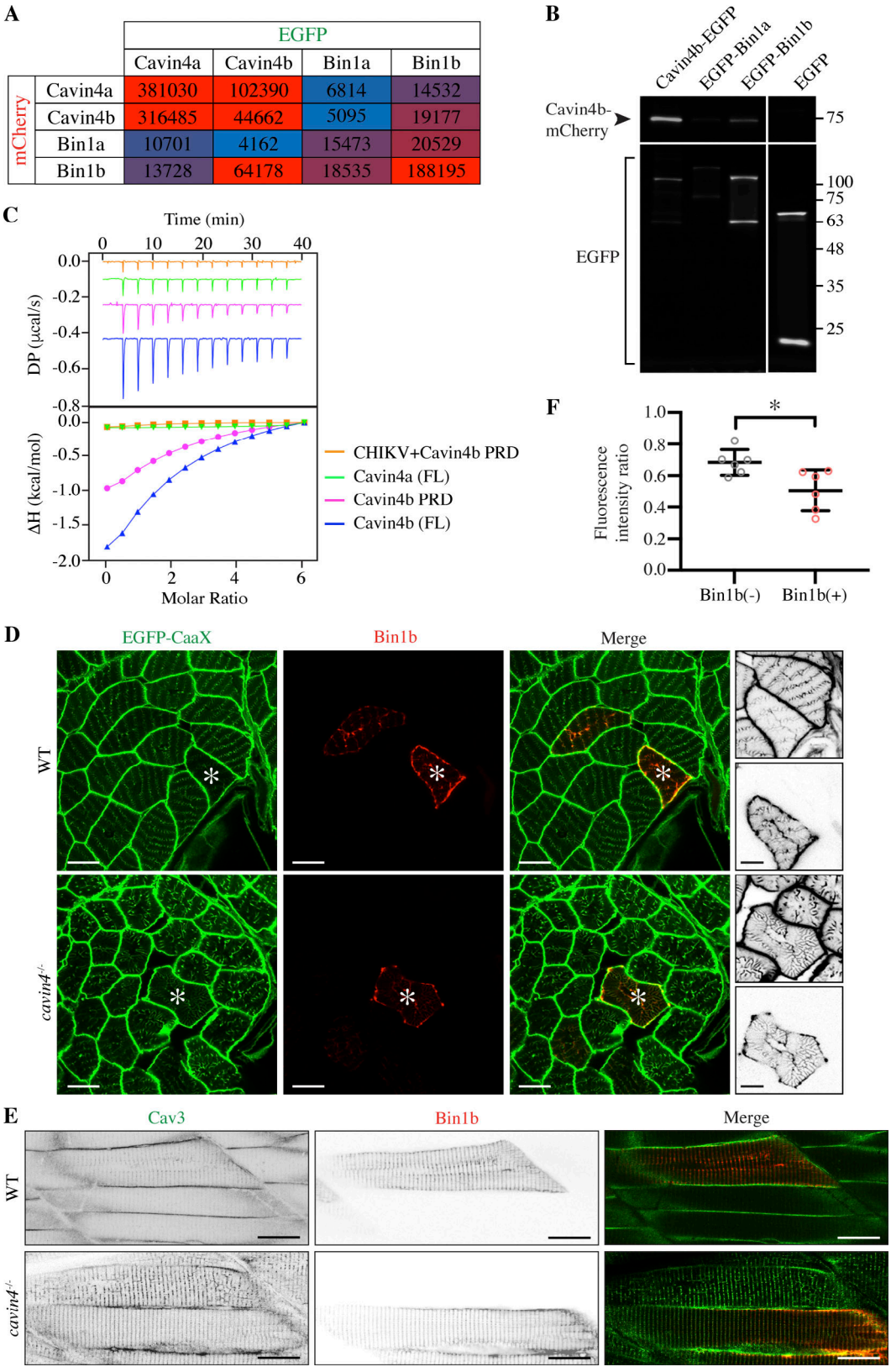

Figure 6. **Cavin4b interacts with Bin1b, and high expression of Bin1b can ameliorate abnormal T-tubule morphology in *cavin4*$^{-/-}$ muscle. (A)** Cell-free expression in *Leishmania* extracts coupled with AlphaLISA showing pairwise comparison of binding between mCherry- and EGFP-tagged Cavin4a, Cavin4b, Bin1a, and Bin1b. Red, positive interaction; blue, no interaction. An arbitrary threshold of 10,000 counts per second of AlphaLISA signal was chosen as the cutoff for a positive interaction. **(B)** Pull-down using GFPtrap with a maltose-binding protein tag with in-gel fluorescence detection after semi-denaturing PAGE. Cavin4b-mCherry was coexpressed with Cavin4b-EGFP (positive control), EGFP-Bin1a, EGFP-Bin1b, or EGFP (reporter only negative control) in BHK

cells. Proteins appear as a doublet due to binding to maltose. Representative blot from three replicates. Molecular weight (kDa) shown on right. See Fig. S5 G for entire gel. **(C)** ITC measurement of Bin1b-SH3 domain with FL Cavin4a, FL Cavin4b, or Cavin4b PRD. Competitive inhibition of Bin1b-SH3/Cavin4b PRD binding was observed by addition of CHIKV PRD. Three replicates performed. **(D)** Confocal images of EGFP-CaaX in transverse sections of WT and *cavin4*$^{-/-}$ skeletal muscle with transient expression of mKate2-Bin1b. Scale bars: 10 µm. Asterisks indicate corresponding muscle fibers; inverted images show a magnification of these fibers (top: EGFP-CaaX; bottom: mKate2-Bin1b; scale bars: 5 µm). **(E)** Live imaging of Cav3-EGFP in 5-dpf WT and *cavin4*$^{-/-}$ embryos with transient expression of mKate2-Bin1b (single channels shown as inverted images). Scale bars: 20 µm. **(F)** Ratio of T-tubule to sarcolemma fluorescence intensity in Bin1b-negative (–) and Bin1b-positive (+) *cavin4*$^{-/-}$ muscle fibers (n = 6 *cavin4*$^{-/-}$ embryos from two independent clutches; two-tailed t test). Colored circles represent individual muscle fibers. *, P ≤ 0.05. Error bars represent mean ± SD.

skeletal muscle and heart tissue, while the profile of caveolar components in zebrafish heart tissue more closely resembled nonmuscle cells. This has implications for the many studies suggesting that caveolar localization is essential for the functioning of components required for cardiac function, including vital modulators of contractility (Balijepalli and Kamp, 2008), and these differences should be considered when using the zebrafish as a model system for caveolar function in the heart. For the purposes of our study, however, a negligible expression level of Cavin4 in the heart allowed us to examine Cavin4 in the zebrafish in a skeletal muscle-specific manner.

Early morphological studies in myotubes and developing muscle fibers proposed that T-tubules develop as interconnected CAV3-positive networks of budding caveolae (Franzini-Armstrong, 1991; Ishikawa, 1968; Parton et al., 1997). We have previously speculated that this accumulation of CAV3/caveolae in T-tubules is a consequence of the similarities in lipid environment of the two domains (Carozzi et al., 2000) and is crucial for the formation of both structures. As CAV3 is restricted to the sarcolemmal caveolae of mature mammalian skeletal muscle, a key stage of T-tubule maturation involves the recycling of CAV3/caveolae back to the sarcolemmal membrane (Parton et al., 1997; Schiaffino et al., 1977). However, the precise mechanisms driving this process remain unknown. The association of caveolae (and their associated protein components) with these precursor T-tubules therefore appears to be an intermediate stage in T-tubule formation, although T-tubule formation is not entirely dependent on caveolae; an absence of CAV3 does not cause loss of T-tubules in mammalian cells and simple eukaryotes, such as *Drosophila*, have a T-tubule system without a detectable caveolin homologue (Galbiati et al., 2001; Kirkham et al., 2008).

Our findings demonstrated a similar transition profile (from T-tubules to sarcolemma) for CAVIN4 in developing mouse muscle. In addition, our transgenic zebrafish lines revealed that Cavin4a and Cav3 show a similar transient association with the early T-tubules, whereas Cavin4b is also present on the T-tubules of more mature fish. Both our CRISPR approach to generate *Cavin4*$^{-/-}$ mouse embryos and our *cavin4*$^{-/-}$ zebrafish line (knocking out both cavin4 paralogs for the first time) revealed striking ultrastructural changes in the absence of Cavin4. The most dramatic findings associated with a loss of Cavin4 were aberrant accumulation of Cav3 in the T-tubules (in both Cavin4-deficient mouse and zebrafish muscle) and fragmentation of the embryonic zebrafish T-tubule network. Consistent with this, electron tomography revealed a striking array of interconnected caveola-like structures in the T-tubules of *cavin4*$^{-/-}$ zebrafish muscle. These lobed bead-like structures extended from the surface several microns into the muscle fiber interior and appear to represent a highly modified T-tubule structure. Aberrant accumulation of Cav3 in the T-tubules was also observed in fish lacking either Cavin4a or Cavin4b, suggesting noncompensatory roles for the two proteins. Although dramatic, *cavin4*$^{-/-}$ fish could nonetheless recover and survive to adulthood. Taken together, our findings suggest a role for Cavin4 in T-tubule stabilization and Cav3/caveolae recycling back to the sarcolemmal membrane.

Cavin4 interacts with Bin1 to enhance T-tubule formation and stability

Here, we demonstrated using multiple approaches that Cavin4 interacts with Bin1, an N-terminal BAR domain protein that plays a fundamental role in T-tubule biogenesis (Lee et al., 2002), and that this interaction occurs between the Bin1b-SH3 domain and the Cavin4b PRD. Using a model cell system, we showed that Cavin4b was both recruited to and increased the formation of Bin1b-induced membrane tubules; this was abolished by mutation of the Cavin4b PRD. This is consistent with published findings showing that SH3 domain ligands can augment the ability of Bin1 to sense and generate membrane curvature (Wu and Baumgart, 2014) and implicates Cavin4 as a positive modulator of Bin1 activity. Cavin4a, which lacks a PRD, was not recruited to Bin1b-positive tubules, raising the possibility that Cavin4a is recruited to T-tubules by Cavin4b or Cav3. In view of this model, we speculated that increased Bin1b expression could rescue the loss of Cavin4 by driving T-tubule tubulation. Indeed, high expression of Bin1b was able to rescue the effect of the loss of Cavin4 in formation of an intact T-tubule network. Interestingly, high Bin1b expression in the absence of Cavin4 was also able to restore Cav3 redistribution to the sarcolemmal membrane, suggesting that Bin1 activity is also required for efficient recycling of T-tubule components from the developing T-tubules and linking the activity of Cavin4 to promoting Bin1-dependent tubulation and in caveolar recycling. The precise mechanisms involved await further mechanistic dissection, but the results are consistent with our observation that a loss of CAVIN4 in mouse muscle led to up-regulation of BIN1 expression, possibly as a compensatory mechanism. However, we observed a higher abundance of longitudinally oriented tubules in juvenile zebrafish (30 dpf), similar to that observed in *Cav3*$^{-/-}$ and *Cavin1*$^{-/-}$ mouse muscle (Galbiati et al., 2001; Lo et al., 2015), which is considered to represent a more immature form of T-tubule structure. Therefore, endogenous levels of Bin1 may not be able to completely compensate for an absence of Cavin4 in T-tubule maturation. Our findings also emphasize the robustness of the development the skeletal

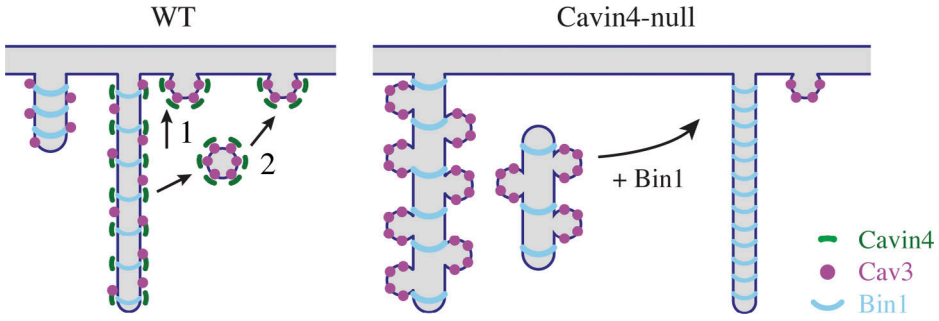

Figure 7. **Model of Cavin4 involvement in T-tubule formation and maturation.** In WT muscle, initial T-tubule formation involves Bin1-mediated membrane deformation. Bin1b recruits Cavin4b through an interaction between the Bin1b SH3-binding domain and the Cavin4b PRD, which enhances T-tubule formation and stabilization. As the T-tubule matures, Cav3 is recycled back to the sarcolemma through a Cavin4-dependent mechanism, either by diffusion within the plane of the membrane (1) or via budding of carriers (2). In the absence of Cavin4, Cav3 accumulates within the T-tubules, generating caveola-like structures, and fragmentation occurs. These aberrant T-tubules can be stabilized by high expression of Bin1, which also promotes redistribution of Cav3/caveolae back to the sarcolemma.

muscle T-tubule system. Indeed, even Bin1 is not essential for T-tubule formation, as down-regulation of dynamin-2 (DNM2) can ameliorate the lethal *Bin1*$^{-/-}$ phenotype in mice (Cowling et al., 2017).

A model for Cavin4 and Bin1 in T-tubule formation and maturation

Our findings suggest a complex interplay between Cavin4 and Bin1. We propose that the interaction of Cavin4 and Bin1 enhances the formation of stable Bin1 tubules, but we have also shown that Cavin4 is required for recycling of Cav3 back to the sarcolemma. We propose a model (Fig. 7) in which the interaction between the Bin1b-SH3 domain and the Cavin4b PRD recruits Cavin4 to the developing T-tubules, which promotes the formation and stabilization of the T-tubules. As the T-tubule matures, Cav3/caveolae are recycled back to the sarcolemmal membrane, but this process is disrupted by loss of Cavin4, leading to a reduction in sarcolemmal caveolae, aberrant accumulation of caveolar structures in the T-tubules, and dysfunctional fragmented T-tubules.

We speculate that Cavin4 could facilitate removal of Cav3 from the developing T-tubules by modifying their architecture or composition, favoring redistribution of Cav3 from the T-tubule system to the sarcolemma through diffusion and exclusion from the T-tubules (pathway 1, Fig. 7) or, alternatively, as part of a pathway in which carriers would bud from the T-tubules to fuse with the sarcolemma (pathway 2, Fig. 7). Pathway 1 relies on a connection to the sarcolemma, which could be disrupted in the fragmented T-tubules of Cavin4$^{-/-}$ muscle, but we propose that fragmentation is an effect of caveola accumulation rather than a cause; i.e., the loss of Cavin4 perturbs the tubules in such a way that diffusion of Cav3 out of the tubule is no longer favored, and the resulting accumulation of Cav3 causes fragmentation. In contrast, pathway 2, the redistribution of Cav3 through budding of carriers, requires fission; in this scenario, Cavin4 could directly participate in recycling back to the sarcolemma (through interactions with Cav3, Cavin1, and fission machinery) or shape the caveolar membrane sufficiently to allow other machinery to associate and cause caveolar budding out of the T-tubule. Importantly, Bin1 overexpression driving tubulation could rescue the aberrant accumulation of Cav3 in Cavin4-deficient T-tubules, raising the possibility that reduced tubulation caused by the loss of the Cavin4/Bin1 interaction also underlies the aberrant accumulation of Cav3. While the precise mechanisms remain to be defined, our results provide an explanation for the association of caveolae with the forming T-tubule system and demonstrate the consequences of a lack of remodeling of this crucial membrane domain. Our models established here provide a means of testing these hypotheses.

In conclusion, we show here a role for Cavin4 and Bin1 in the remodeling of the T-tubule system in developing skeletal muscle. The interaction between Cavin4 and Bin1 identified in this study also highlights a potential role for Cavin4 as a genetic modifier in BIN1- and DNM2-related myopathies.

Materials and methods

Animal maintenance

WT mice (C57/bl6) were housed according to institutional guidelines (The University of Queensland), with food and water available ad libitum. Zebrafish were maintained according to institutional guidelines (The University of Queensland). All zebrafish were maintained on the Tuebingen/AB background. Zebrafish embryos were raised at 28.5°C in standard E3 (5 mM NaCl, 0.17 mM KCl, 0.33 mM $CaCl_2$, and 0.33 mM $MgSO_4$). All animal experiments were approved by The University of Queensland Ethics Committee and University of Queensland Biosafety Committee.

Antibodies

The following antibodies were used: mouse anti-β-dsytroglycan (7D11; Developmental Studies Hybridoma Bank), rabbit anti-CAV3 (peptide sequence CGFEDVIAEPEGTYSFDE; Luetterforst et al., 1999), mouse anti-CAV3 (#610421; BD Biosciences), rabbit anti-Cavin4 (peptide sequence CGDDESLLLELKQSS; Lo et al., 2015), rabbit anti-Cavin4b (peptide sequence GEESEVPMYDMKQLS), mouse anti-BIN1 (clone 99D, #05-449-C; Millipore),

mouse anti-actin (α-sarcomeric; clone 5C5 #A2172; Sigma-Aldrich), anti-rabbit Alexa Fluor 555 secondary antibody (#A-31572; Invitrogen), and anti-mouse Alexa Fluor 488 secondary antibody (#A-21202; Invitrogen).

DNA constructs

A list of constructs generated for this study can be found in Table S1.

Stable transgenic zebrafish lines

For this study, the *Tg(acta1*:GCaMP5)^{uq16rp} line was generated using the Tol2 transposon system (Kawakami, 2007; Kwan et al., 2007; Villefranc et al., 2007). Briefly, one-cell-stage zebrafish embryos were microinjected with 50 ng/µl plasmid vector and 25 ng/µl transposase RNA. Transgenics were crossed until Mendelian frequencies were reached, indicative of single genomic integrations. Existing transgenic lines used in this study were *Tg(actc1b*:Cavin4a-clover)^{uq17rp} (Xiong et al., 2021), *Tg(actc1b*:Cavin4b-clover)^{uq18rp} (Xiong et al., 2021), *Tg(actc1b*:Cavin1a-clover)^{uq19rp} (Xiong et al., 2021), *Tg(actb2:EGFP-CAAX)*^{pc10} (Williams et al., 2011), and *Tg(cav3*:Cav3GFP)^{uq11rp} (Gormal et al., 2020; Lo et al., 2015). Stable lines were maintained as heterozygotes.

qRT-PCR

Total RNA from adult zebrafish and mouse tissues was isolated using TRIzol reagent (#15596026; Invitrogen), treated with Turbo DNase (Turbo DNA-free kit, # AM1907; Invitrogen), and RNA purified using the Qiagen RNeasy mini kit (#74104; Qiagen), all according to the manufacturer's instructions. Total RNA from zebrafish embryos and C2C12 cells was isolated using the RNeasy mini kit (#74104; Qiagen) according to the manufacturer's instructions. 1 µg RNA was transcribed into cDNA using the Superscript III First-Strand Synthesis System (#18080051; Invitrogen) according to the manufacturer's instructions. qRT-PCR was performed using the SYBR green PCR master mix (#4309155; Applied Biosystems) on an Applied Biosystems ViiA7 real-time PCR system, and gene expression data were analyzed using the ΔΔCt method. PCR primers were purchased from Sigma-Aldrich; sequences are provided in Table S2.

Whole-mount ISH

Cavin4a and *cavin4b* constructs were purchased from Integrated Sciences (IMAGE clones 7252030 and 7052606, respectively) and subcloned into pBluescript. The *cavin4a* and *cavin4b* probes were synthesized by in vitro transcription using T3 polymerase (#AM1348; Life Technologies) and DIG RNA labeling mix (#11277073910; Roche Diagnostics). The *anp* probe was from Smith et al. (2011). Zebrafish embryos were dechorionated, fixed in 4% PFA and stored in methanol at −20°C until required. ISH was then performed as described in Thisse and Thisse (2008), with minor modifications. Briefly, embryos were rehydrated back into 100% PBST (PBS/0.1% Tween 20), and embryos older than 24 hpf were permeabilized in 10 µg/ml Proteinase K solution (#25530015; Invitrogen; 8 min for 24-hpf embryos, 28 min for 48-hpf embryos, and 30 min for 5-dpf and 7-dpf embryos). Embryos were postfixed in 4% PFA for 20 min and washed 2 × 5 min in PBST, followed by prehybridization at 65°C for 1 h in hybridization buffer (HYB; 50% formamide, 5X SSC, 50 µg/ml heparin, 500 µg/ml tRNA, 0.1% Tween 20, and 9 mM citrate). Embryos were incubated in probe in HYB overnight at 65°C, then washed at 65°C for 10 min in 70% HYB/30% 2X SSC, 10 min 30% HYB/70% 2X SSC, 10 min in 2X SSC, 2 × 15 min in 0.2X SSC, 2 × 15 min 0.05X SSC. Further washing was performed at RT for 5 min in 70% 0.05X SSC/30% PBST, 5 min in 30% 0.2X SSC/70% PBST, and 5 min in PBST, followed by blocking for 1 h in PBST with 2% BSA, 2% horse serum. Embryos were incubated overnight at 4°C with preabsorbed alkaline phosphatase–coupled anti-digoxigenin antibody (#11093274910; Roche Diagnostics) diluted in blocking solution. Embryos were washed 6 × 15 min in PBST at RT and developed in nitro blue tetrazolium/5-bromo-4-chloro-3-indolyl-phosphate (NBT/BCIP) solution (#11681451001; Roche Diagnostics). Reaction was stopped in 1X PBST, and embryos were refixed in 4% PFA overnight at 4°C and cleared in methanol. Embryos were mounted in glycerol and images captured on an Olympus SZX-12 stereomicroscope with an Olympus DP-71 12 Mp color camera using DP capture software. Adjustments of brightness and contrast were applied using Adobe Photoshop software.

Cell culture

C2C12 cells (ATCC CRL-1772) and BHK cells (ATCC CCL-10) were maintained in DMEM containing 10% FBS (#F31803; Cell Sera) and 5 mM L-glutamine (#25030-081; Invitrogen) at 37°C under 5% CO_2. Cells were routinely screened for mycoplasma using a MycoAlert Mycoplasma detection kit (#LT07-418; Lonza). C2C12 cells were seeded onto Matrigel-coated (#356234; BD Biosciences) 60-mm dishes (#150462; Thermo Scientific) or Ibidi µ-slide 8-well tissue culture–treated chambers (#50001; DKSH Australia). Cells were induced to differentiate by replacing 10% FBS with 2% horse serum (#26050070; Invitrogen) in the growth medium, and cells were cultured for another 4 d. BHK cells were seeded onto 35-mm Ibidi glass-bottom dishes (#81218-200; DKSH Australia) and transfected with DNA constructs using Lipofectamine 3000 (#L3000015; Invitrogen) at 70% confluence according to the manufacturer's instructions.

Live confocal imaging of BHK cells was performed at 37°C on a Zeiss Inverted LSM880 with fast Airyscan detector at 37°C using a 40× Plan Apochromat objective (NA 1.3). At 18 h after transfection, cell culture medium was replaced with phenol red–free DMEM/F12 medium (#11039-021; Invitrogen) containing 10% FBS 1 h before imaging. T-tubule dynamics were tracked for 6 min with a 3-s interval, and images were processed using Fiji (ImageJ). Bin1b-induced tubules were analyzed using the analyze particles function. Hyperstacks of 51 frames were temporally color coded to visualize the dynamic tubules.

Western blot analysis

Samples were homogenized using a IKA T10 basic Ultra-Turrax homogenizer in ice-cold RIPA buffer (50 mM Tris-HCl, pH 8.0, 150 mM NaCl, 1% NP-40, 0.5% sodium deoxycholate, 0.1% sodium dodecyl sulfate, and 1 mM EDTA) containing Protease Inhibitor cocktail set III (#539134; Merck Millipore) and immediately supplemented with 4X Laemmli's sample buffer

(240 mM Tris-HCl, pH 6.8, 40% glycerol, 8% sodium dodecyl sulfate, and 0.04% bromophenol blue) and 10 mM DTT. Protein concentrations were determined using the Pierce bicinchoninic acid protein assay kit (#23225; Thermo Scientific). Proteins were resolved by 10% SDS-PAGE and transferred to Immobilon-P polyvinylidene difluoride membrane (#IPVH00010; Merck Millipore). Proteins were visualized with horseradish peroxidase (HRP)-conjugated secondary antibodies and the Clarity Western ECL substrate (#1705060, Bio-Rad Laboratories) and imaging captured using the Bio-Rad ChemiDoc MP system as per the manufacturer's instructions. Anti-mouse (#G21040) and anti-rabbit (#G21234) HRP-conjugated antibodies were from Invitrogen.

CRISPR-Cas9–based generation of *Cavin4*$^{-/-}$ mice and C2C12 cells

Cavin4$^{-/-}$ C2C12 cells and mice were generated at the Queensland Facility for Advanced Genome Editing and Genome Innovation Hub, The University of Queensland. For *Cavin4*$^{-/-}$ C2C12 cells, four highly specific guide RNAs (gRNAs) targeting the first coding exon of mouse Cavin4 were designed using the online program CRISPOR (Concordet and Haeussler, 2018). The sequences were as follows: gRNA1, 5′-CTACGCCTGGAGCCAAAAGT-3′; gRNA2, 5′-GAATCGGTTGTCAAGTGTGA-3′; gRNA3, 5′-TGTGACCGTGCTGGACAGAG-3′; gRNA4, 5′-GGCCCGGGTAGAGAAGCAAC-3′. For CRISPR delivery, synthetic gRNA (CRISPR RNA/trans-acting CRISPR RNA duplex, 10 pmol each; IDT) were mixed with spCas9 protein (IDT) at 1:1 ratio and transfected into 100,000 C2C12 cells by electroporation (#MPK1025 Neon transfection kit; Invitrogen) using the following parameters: 1,650 V, 10 ms, three pulses. Editing efficiency of bulk cell pools was confirmed by T7E1 (T7 Endonuclease I, #M0302S; NEB) assay, followed by single-cell cloning using limited dilution in a 96-well plate. Genomic sequence of isolated clones at targeting locus were further confirmed by PCR cloning (#E1202S; NEB) and Sanger sequencing (Australian Genome Research Facility, The University of Queensland). A single clonal line harboring a homozygous 155-bp deletion was chosen for further study.

To maximize homozygous reading frameshift mutations in *Cavin4*$^{-/-}$ mouse embryos, two gRNAs targeting the first exon and one gRNA targeting the first intron of Cavin4 were designed for codelivery. The sequences were as follows: gRNA1, 5′-TGTGACCGTGCTGGACAGAG-3′; gRNA2, 5′-GGCCCGGGTAGAGAAGCAAC-3′; gRNA3 (intronic), 5′-TGGACACCCCTGTGACTCGG-3′. The efficiency of gRNAs were first validated in mouse embryonic fibroblasts before CRISPR mice experiment. Animal breeding and microinjection was performed at the Transgenic Animal Service of Queensland, The University of Queensland. For microinjection, 1 µM each of gRNA (IDT) was mixed with spCas9 at 3:2 ratio in embryo-grade water (#W1503; Sigma-Aldrich) and injected into WT C57BL6 zygotes at the one-cell stage. Tissue samples of F0 animals were collected at postnatal day 3. Mouse muscle was removed and flash frozen in liquid nitrogen or fixed (in 4% PFA/PBS for cryosectioning or 2.5% glutaraldehyde/PBS for EM). Genomic DNA was extracted from nonmuscle tissue and PCR performed to identify animals carrying homozygous deletions at the target region. Reading frameshift mutations and modified sequence were further validated by PCR cloning and Sanger sequencing. Mouse genomic PCR primers (Sigma-Aldrich) were as follows: 5′-AGAGAAAAACTTAGTTCAGTGTTTGAAG-3′ and 5′-ACAGTTCACATTCCATGACTAATAAGAA-3′.

Immunofluorescence

C2C12 myotubes were fixed in 4% PFA and permeabilized with 0.1% Triton X-100, followed by blocking in 0.2% fish skin gelatin/0.2% BSA. Cells were then incubated in primary antibodies (diluted in blocking solution), followed by incubation in secondary antibodies and mounting in Mowiol (#475904; Merck). Confocal images were captured on a Zeiss Axiovert 200 upright microscope stand with LSM 710 meta confocal scanner (63× Plan Apochromat objective NA 1.4). Images were processed in Fiji (ImageJ) and adjustments of brightness and contrast applied in Adobe Photoshop.

PFA-fixed mouse muscle tissue was washed three times in PBS, acclimated from 15% to 30% sucrose/PBS, and then frozen in a dry-ice ethanol bath in Tissue-Tek OCT compound (#IA018; ProSciTech). 5-µm cryosections were cut on a Leica cryostat and transferred to Superfrost-Plus microscope slides (#EPBRSF41296SP; Thermo Scientific). Sections were dried at 65°C for 2 h, washed in PBS, and permeabilized with 0.1% Triton X-100, followed by blocking in 2% BSA. Sections were then incubated in primary antibody (diluted in blocking solution), followed by incubation in secondary antibody and mounting in Mowiol (#475904; Merck). Alexa Fluor 488–conjugated Phalloidin (#A12379) was from Invitrogen. Confocal images were captured on a Zeiss Axiovert 200 upright microscope stand with LSM710 meta confocal scanner (63× Plan Apochromat objective NA 1.4). For fluorescence intensity CAV3 measurements, samples were coded (blinded) and intensity measured using freehand selection in Fiji (ImageJ) of sarcolemmal and internal staining areas for five muscle fibers per image. Images were processed in Fiji (ImageJ) and adjustments of brightness and contrast applied in Adobe Photoshop.

Live imaging of zebrafish embryos

For transient expression, DNA was injected into zebrafish embryos at a concentration of 20 ng/µl, and embryos expressing the fluorescently tagged protein of interest were chosen before imaging.

Zebrafish embryos were anesthetized in tricaine (#A5040; Sigma-Aldrich)/E3 solution and mounted in 1% low-melting-point agarose (#A9414; Sigma-Aldrich). Confocal images of mounted embryos (immersed in tricaine/E3) were captured on a Zeiss Axiovert 200 upright microscope stand with LSM710 meta confocal scanner (40× Plan Apochromat water immersion objective NA 1.0) or Zeiss Axiovert 200 inverted microscope stand with a laser scanning microscope 710 confocal scanner (63× long working distance C-Apochromat objective NA 1.15). Images were processed in Fiji (ImageJ) and adjustments of brightness and contrast applied in Adobe Photoshop.

For Cavin1a-Clover, Cavin4a-Clover, and Cavin4b-Clover transgenic lines, the fluorescence intensity of T-tubules was calculated by measuring mean gray value of 11 individual T-tubules per muscle fiber using line scale in ImageJ. The fluorescent intensity of the sarcolemma was measured by mean gray value of the sarcolemma connected by the 11 T-tubules.

The *cavin4a*$^{-/-}$, *cavin4b*$^{-/-}$, and *cavin4*$^{-/-}$ mutant lines were crossed into the *Tg(cav3*:Cav3GFP)^{uq1rp} background. Cav3GFP-expressing heterozygotes were then crossed with respective *cavin4a*$^{-/-}$, *cavin4b*$^{-/-}$, and *cavin4*$^{-/-}$ fish. The resulting embryos, along with Cav3GFP-expressing WT embryos, were imaged as described above, and embryos were genotyped after imaging to identify homozygous mutants. Quantitation of T-tubule versus sarcolemmal intensity was calculated by highlighting a rectangular area within the relevant area and using ImageJ to measure mean gray values. The ratio of T-tubule to sarcolemmal fluorescence intensities was calculated by averaging the mean gray value from at least three different muscle fibers in a single embryo.

EM

Mouse muscle tissue and zebrafish embryos were processed for EM as described in Lo et al. (2015) using a modification of the method by Nguyen et al. (2011). Briefly, tissue was immersed in a solution of 2.5% glutaraldehyde in PBS and immediately irradiated in a Pelco Biowave (Ted Pella) for 3 min at 80 W under vacuum. Samples were transferred to a fresh solution of 2.5% glutaraldehyde in PBS and left for 30 min at RT before washing in 0.1 M cacodylate buffer. Samples were then immersed in a solution containing potassium ferricyanide (3%) and osmium tetroxide (2%) in 0.1 M cacodylate buffer for 30 min at RT and then in a filtered solution containing thiocarbohydrazide (1%) for 30 min at RT, osmium tetroxide (2%) for 30 min, and in 1% aqueous uranyl acetate for 30 min at 4°C. After a further staining step of 20 min in 0.06% lead nitrate in aspartic acid (pH 5.5) at 60°C, samples were dehydrated and embedded in epon LX112 resin (#21310; Ladd Research). The density of caveolae was determined using standard stereological methods on randomly chosen sections (Parton, 1994).

For serial blockface sectioning, serial thin sections (50 nm) were cut and imaged on a 3View serial blockface scanning electron microscope in backscatter detection mode (Ariotti et al., 2015). Images were aligned using the program xfalign in IMOD and segmented (Noske et al., 2008).

Electron tomography was done following the procedures previously described (Richter et al., 2008). In brief, for data acquisition, a Tecnai G2 F30 transmission EM operated at 300 kV and equipped with a Gatan K2 summit direct electron detector was used. Dual-axis tilt series were acquired in linear imaging mode over a total tilt angle of ±60° with increments of 1°. Serial EM was used as microscope control and imaging software (Mastronarde, 2005). Reconstructions were generated by using radially weighted back-projection as implemented in IMOD followed by semiautomated segmentation (Noske et al., 2008).

CRISPR-Cas9 generation of *cavin4a*$^{-/-}$ zebrafish line

Target site selection for zebrafish *cavin4a*-specific sgRNA was determined using the webtool CHOPCHOP (Montague et al., 2014). Targets with more than 50% G/C content and no predicted off-target site were chosen. The chosen target sequence with juxtaposed protospacer adjacent motif sequence of *cavin4a* is as follows: GGAACGCCAACAGCAGCTCGAGG, genomic location chr2:42292952. The method for cloning-independent synthesis of sgRNA was adopted from Gagnon et al. (2014) and performed as described previously (Lim et al., 2017). Briefly, *cavin4a*-specific sgRNA was produced by incubating the gene-specific and constant oligonucleotides together in an annealing reaction in a Veriti 96-Well Thermal Cycler as follows: 95°C 5 min, 95°C to 85°C (−2°C/s), 85°C to 25°C (−0.1°C/s). Next, a fill-in reaction was performed, and 10 mM dNTP, NEB buffer 2, 100x BSA, and T4 DNA polymerase (#M0203S; NEB) were added to the annealing reaction and incubated for 20 min at 12°C. The resulting DNA template was purified using the QIAquick PCR Purification Kit (#28104; Qiagen) and verified by agarose gel electrophoresis. Following, sgRNA was transcribed using the Ambion MEGAshortscript T7Transcription Kit (#AM1354; Thermo Scientific) with Turbo DNase (Turbo DNA-free kit, #AM1907; Invitrogen) incubation (15 min, 37°C) and purified using Zymo Research RNA Clean & Concentrator Kit (#R1015; Zymo Research). An injection mixture containing 700–753 ng/µl recombinant Cas9 protein (#CP01-50; PNA Bio) 200–208 ng/µl sgRNA and 16% phenol red (#P0290; Sigma-Aldrich) was prepared and incubated for 5 min at RT to allow for Cas9–sgRNA complex formation, followed by injection into one-cell stage WT embryos. Stable *cavin4a* F1 mutant zebrafish lines were identified by Sanger sequencing using the following primers: 5′-TGC GTTTGAGTCCCTTTACC-3′ and 5′-GCACACCCTCATTCACCA AT-3′ (Sigma-Aldrich). The *cavin4a*^{uq5rp} mutant was identified and bred to homozygosity. Mutants were confirmed by Sanger sequencing (Australian Genome Research Facility, Brisbane) or restriction digest with BglI (#R0143S; NEB).

TILLING (targeting induced local lesions in genomes) mutagenesis screen for identification of *cavin4b*$^{-/-}$ zebrafish line

The *cavin4b*^{uq6rp} mutant was identified by screening an N-ethyl-N-nitrosourea mutagenesis zebrafish library at the Hubrecht Institute, Utrecht, Netherlands (Wienholds et al., 2003), with the primers 5′-TAAAGAGAAACCCACCGAAG-3′ and 5′-ATGTCA CCACACATTTAGGCC-3′ (Sigma-Aldrich), and bred to homozygosity. Subsequent genotyping of this line was performed using the primers 5′-AGCGCCATGAACATCTTCTCT-3′ and 5′-CTG GTAGATGACGACACGGAA-3′ (Sigma-Aldrich); mutants were confirmed by Sanger sequencing (Australian Genome Research Facility, Brisbane) or digestion with αTaqI (#R0149S; NEB).

Morphometrics of live zebrafish

Images of anesthetized embryos were captured on an Olympus SZX12 stereomicroscope with a Olympus DP70 CCD camera using DP capture software. Images were processed in Fiji (ImageJ) and adjustments of brightness and contrast applied in Adobe Photoshop. Body length (BL) was determined using Fiji (ImageJ).

Birefringence imaging was performed on anesthetized embryos using a Nikon SMZ1500 stereomicroscope with two polarizing light filters with their axes of polarization oriented 90°C from each other (Berger et al., 2012; Telfer et al., 2010) using NIS Elements software. Automated quantitation of mean gray value was determined using custom ImageJ macros. The full codes for generating region of interest (Data S1) and mean gray value (Data S2) have been provided.

Vibratome sectioning

For embryos genotyped before imaging, DNA was isolated by transection of the embryonic tail fin within the pigment gap distal to the circulating blood (Wilkinson et al., 2013) in 72-hpf embryos, followed by genotyping analysis for *cavin4a* and *cavin4b* as described above. Zebrafish embryos were fixed in 4% PFA overnight at 4°C and mounted in 8% low-melting-point agarose (#A9414; Sigma-Aldrich). Vibratome sections were cut to a thickness of 100 µm using a Leica VT1000S vibratome and mounted in Mowiol (#475904; Merck). Confocal images were captured on a Zeiss Axiovert 200 upright microscope stand with LSM710 meta confocal scanner (63× Plan Apochromat objective NA 1.40). Images were processed in Fiji (ImageJ) and adjustments of brightness and contrast applied in Adobe Photoshop.

Zebrafish muscle fiber isolation

Muscle fibers were isolated from 4-dpf zebrafish embryos as described in Nixon et al. (2005). Briefly, fibers were dissociated using 3.125 mg/ml collagenase type II (#CLS-2; Worthington Biochemical) in CO_2-independent medium (#18045088; Gibco) at 37°C for 1.5 h. Muscle fibers were triturated and centrifuged at 380 *g* for 1 min; supernatant was removed, and fibers were resuspended in CO_2-independent medium. Fibers were allowed to settle on poly-L-lysine (#P8920; Sigma-Aldrich)–coated 12-mm Menzel-Glaser glass coverslips (#EPBRCSC121GP; Bio-Strategy), fixed in 4% PFA, and labeled as per the above immunofluorescence protocol with primary antibodies and DAPI (#D9542; Sigma-Aldrich) counterstain. Muscle fibers were examined using an Olympus BX-51 upright microscope with Olympus DP70 CCD camera (60× objective NA 1.35). In Cav3-immunolabeled fibers, individual noncontracted muscle fibers were selected via the freehand selection tool and measured for integrated density via Fiji (ImageJ). Background value was determined as a product of mean gray value and the mean area of selected regions surrounding a particular fiber. To measure the corrected total cell fluorescence (CTCF) of each fiber, the integrated density of each fiber was subtracted with its corresponding background value.

Embryo swimming analysis

Zebrafish embryos were placed into 24-well plates (#142475; Thermo Scientific; one embryo per well), incubated at 28°C, and analysis was performed using the Zebrabox (Viewpoint; http://www.viewpoint.fr/en/p/equipment/zebrabox) according to the manufacturer's instructions and as performed in Giacomotto et al. (2015). Briefly, plates were incubated in the dark for 1 h, followed by recording of swimming behavior for 10 min under light. Data were exported and processed using Microsoft Excel.

Swim tunnel assessment

6-mo-old male WT and *cavin4b*$^{-/-}$ zebrafish were immobilized in tricaine. BL (measured from the snout to tip of zebrafish before caudal fin) was measured, and zebrafish were allowed to recover for 30 min. Individual zebrafish were acclimatized for 10 min in the swimming chamber (#SW10050; Loligo Systems) illuminated in the forward swimming direction. The swim tunnel assessment was started at a water flow speed of 150 rpm for 10 min. Water flow was subsequently increased by a function of the BL of individual zebrafish every 10 min until fatigue (defined as the inability of the zebrafish to remove itself from the downstream mesh screen for more than 5 s) was observed. A standard curve of water velocity (centimeters per second) was generated using handheld digital flow meter (#AC10000; Loligo Systems) and vane wheel probe (#AC10002; Loligo Systems). Water in the swim tunnel was heated to ∼25°C using standard aquarium water heaters. The critical swimming speed (Ucrit) was calculated using the following equation:

$$\text{Ucrit} = \text{Ui} + [\text{Uii} / (\text{Ti}/\text{Tii})],$$

where Ui denotes the highest speed successfully maintained throughout the series of 10-min intervals, Uii denotes the speed increment (linear function of the BL of individual zebrafish), Ti represents the fraction of the 10-min interval elapsed upon fatigue, and Tii represents the period of time interval (10 min; Plaut, 2000).

In vivo Ca^{2+} imaging in zebrafish embryos

The *cavin4*$^{-/-}$ mutant line was crossed into the *Tg(acta1*:GCaMP5)^{uq16rp} transgenic line. GCaMP-positive *cavin4*$^{-/-}$ embryos were generated from homozygote × heterozygote crosses. Homozygous *cavin4*$^{-/-}$ embryos were identified by transection of the embryonic tail fin within the pigment gap distal to the circulating blood (Wilkinson et al., 2013) in 72-hpf embryos, followed by genotyping analysis for *cavin4a* and *cavin4b* as described above. Individually anesthetized embryos were mounted in 1% low-melting-point agarose (#A9414; Sigma-Aldrich) in a Petri dish and electrically stimulated using a Square Pulse Stimulator S44 (Grass Instruments). Electrical stimulation settings were as follows: 1-ms pulse every 4 s, 80 V, minimum delay (1 × 0.01 ms). Images were captured on a Zeiss Axiovert 200 upright microscope stand with LSM 710 meta confocal scanner (20× water immersion objective, NA 0.5) in line scan mode at a sampling rate of 5000 measurements over 40 s. Fluorescence intensities were analyzed in Microsoft Excel. For analysis, the average values were calculated for every 10th measurement, giving a total of 500 measurements. Amplitude (ΔF/F) was calculated using the equation (Fmax − Fmin)/Fmin, where Fmax is the maximum intensity and Fmin is the background, and was determined using the MAX:MIN function in Microsoft Excel. Decay of signal (half-life) was determined using the single-exponential decay function in GraphPad Prism. Average amplitude and decay per embryo were determined using the second response peak after application of stimulation and was calculated as the mean of a minimum of three different muscle fibers from a single embryo.

Cell-free protein expression–coupled AlphaLISA

Open reading frames were cloned into cell-free expression vectors containing Species Independent Translation Initiation Sequence and fluorescent tags using the Gateway cloning system (Johnston et al., 2019). The coexpression of proteins in the *L. tarentolae* cell-free expression system was performed as described in Varasteh Moradi et al. (2020). In brief, the DNA templates for GFP and mCherry fusion proteins (20 nM and 40

nM, respectively) were added concomitantly to the *L. tarentolae* cell-free expression reaction mixture, and samples were incubated for 4 h at 27°C for expression. The quality of expressed proteins was examined by semi-denaturing SDS-PAGE imaged by ChemiDoc MP system (Bio-Rad). For AlphaLISA assay, protein samples were diluted 25 times in buffer A (25 mM Hepes, 50 mM NaCl, 0.1% BSA, and 0.01% vol/vol Nonidet, pH 7.5). Biotinylated mCherry nanobody (1 µl, diluted in buffer A to a final concentration of 4 nM) was added to a 384-well microplate (OptiPlate-384 Plus; Perkin Elmer) followed by the addition of 15 µl diluted proteins and 5 µl of the GFP antibody-conjugated acceptor beads (5x). The mixture was incubated for 30 min at RT. Subsequently, 5 µl of streptavidin-coated donor beads (5x) were added to samples under low-light conditions and incubated for 30 min at RT. The AlphaLISA signal was detected with the Tecan Spark multimode microplate reader using the following settings: mode, AlphaLISA; excitation time, 130 ms; integration time, 300 ms. Each protein pair was tested in triplicate, and the detected Alpha signal values reported are the mean of three measurements.

Recombinant protein transformation and expression

N-terminally histidine (His)-tagged Bin1b SH3 from zebrafish was cloned into pET-28a (+) expression vector (GenScript). FL zebrafish Cavin4a (Cavin4a-FL) and Cavin4b (Cavin4b-FL) were both cloned using the overlap extension PCR method into a pHUE expression vector at SacII restriction enzyme site with N-terminal 6 × His-ubiquitin tag. The Bin1b-SH3 construct was transformed into *Escherichia coli* Rosetta 2 (DE3) competent cells (#71403; Novagen, Merck) by heat shock. Cavin4a-FL and Cavin4b-FL constructs were transformed into *E. coli* strain BL21 CodonPlus (DE3) competent cells (#230280; Integrated Sciences). Cells were propagated in LB media and recombinant protein expression performed by inducing with 500 µl (0.5 mM) IPTG (#BIO-37036; Bioline) at 18°C overnight (~20 h). The resultant cell culture was harvested in 50 mM Hepes, pH 7.4, 100 mM NaCl, and 5 mM imidazole buffer (Binb-SH3 domain expression) or 20 mM Hepes, pH 7.4, 500 mM NaCl, and 5 mM imidazole buffer (Cavin4a-FL and Cavin4b-FL) with addition of benzamidine hydrochloride and DNase.

Recombinant protein purification

Harvested cells were lysed by high-pressure homogenization using a continuous flow cell disruptor (Constant Systems) at 32 kPsi at 5°C with addition of 0.5% wt/vol Triton X-100 followed by 30 min high-speed centrifugation at 38,000 *g* using Beckman JA 25.5 rotor. The supernatant was incubated with preequilibrated specific TALON metal affinity resin (#635503; ClonTech, Scientifix) for 1 h with continuous stirring at 4°C. The His-tagged SH3 domain bound with TALON resin was washed with 50 mM Hepes, pH 7.4, 100 mM NaCl, and 5 mM imidazole and eluted by 50 mM Hepes, pH 7.4, 100 mM NaCl, and 300 mM imidazole. The His-ubiquitin–tagged Cavin4a-FL and Cavin4b-FL proteins bound with TALON resin were washed with 20 mM Hepes, pH 7.4, 500 mM NaCl, and 5 mM imidazole and eluted by 20 mM Hepes, pH 7.4, 500 mM NaCl, and 300 mM imidazole. The eluted Binb SH3 sample was immediately loaded on size exclusion chromatography column HiLoad 16/600 Superdex 75 prep grade column (GE Healthcare) preequilibrated with 0.22-µm filtered 50 mM Hepes, pH 7.4, and 100 mM NaCl buffer containing 1 mM DTT. The eluted Cavin4a-FL and Cavin4b-FL proteins were loaded on size exclusion chromatography column Superose 6 Increase 10/300 GL column (GE Healthcare) preequilibrated with 0.22-µm filtered 50 mM Hepes, pH 7.4, 100 mM NaCl, and 1 mM DTT buffer.

ITC

The CHIKV and zebrafish Cavin4b proline-rich peptides were synthesized by GenScript and dissolved in sterile water to a concentration of 6 mM stock solution. The peptide pH was adjusted to neutral by mixing 10 µl of 6 mM peptide stock with 5 µl buffer containing of 150 mM Hepes, pH 8.0, 300 mM NaCl, and 3 mM DTT to a final concentration of 600 µM with a neutral pH containing 50 mM Hepes, 100 mM NaCl, and 1 mM DTT buffer for downstream ITC experiments. All microcalorimetry experiments of zebrafish Bin1b SH3 domain were determined using a MicroCal iTC200 calorimeter (Malvern) at 25°C. The ITC experiments were performed with one single 0.4-µl injection followed by 12 injections of 3.22 µl each with stirring speed of 750 rpm and 180 s injection spacing. All peptides were dissolved in the same buffer before ITC experiments. 600 µM CHIKV peptide or 600 µM Cavin4b peptide was titrated into 20 µM Bin1b SH3 solution in the sample cell containing the same buffer (50 mM Hepes, pH 7.4, 100 mM NaCl, and 1 mM DTT). The competitive ITC experiments were conducted by titrating 600 µM Cavin4b peptide into 20 µM Bin1b SH3 with 20 µM CHIKV peptide preincubated on ice for 30 min. To examine the interaction of Bin1b SH3 domain and FL Cavin4a and Cavin4b protein, 600 µM Bin1b SH3 was titrated into 20 µM Cavin4a and Cavin4b FL proteins, respectively, containing 50 mM Hepes, pH 7.4, 100 mM NaCl, and 1 mM DTT. Thermodynamic profiles were generated using Prism 8. The experiment was conducted with three technical replicates.

GFP-trap pull-down with in-gel fluorescence

BHK cells were transfected as described above. At 16 h after transfection, cells were lysed in NP-40 buffer (50 mM Tris-HCl, 150 mM NaCl, 1% NP-40, and 5 mM EDTA), supplemented with cOmplete Protease Inhibitor Cocktail (#11836145001; Sigma-Aldrich) at 4°C. Cells in lysis buffer were disrupted with a 25-gauge needle syringe (~15 times) and incubated on ice for 30 min. Samples were spun at 14,000 *g* for 10 min at 4°C, and the cleared lysates were incubated with amylose resin (#E8021L; NEB) precoated with MBP-tagged GFPtrap beads for 1 h at 4°C. After incubation, amylose resin was separated from solution by centrifugation at 2,000 *g* for 3 min and washed three times with lysis buffer. The GFP-MBP and its captured proteins were eluted from amylose resin by 10 mM maltose in lysis buffer. The eluted proteins were separated by semi-denaturing PAGE followed by in-gel fluorescence with the ChemiDoc MP system (Bio-Rad) as per the manufacturer's instruction.

Statistical analyses

Statistical analyses were performed using Microsoft Excel and GraphPad Prism (GraphPad). All error bars represent mean ±

SD. For comparison between two groups, P values were determined using a two-tailed *t* test. For comparison of more than two groups, one-sided ANOVA tests were conducted with Tukey's or Dunnett's multiple-comparison test. P values less than 0.05 were considered statistically significant. Data distribution was assumed to be normal, but this was not formally tested.

Online supplemental material

Fig. S1 shows characterization of Cavin4 expression in zebrafish and characterization of *Cavin4*$^{-/-}$ mouse muscle and *Cavin4*$^{-/-}$ myotubes. Fig. S2 shows generation and characterization of single *cavin4a*$^{-/-}$ and *cavin4b*$^{-/-}$ zebrafish lines. Fig. S3 shows further characterization of the *cavin4b*$^{-/-}$ zebrafish line. Fig. S4 shows T-tubule structure of cavin4$^{-/-}$ muscle at different developmental stages and high expression of Bin1b in cavin4$^{-/-}$ muscle fibers. Fig. S5 shows ultrastructure of *cavin4*$^{-/-}$ muscle and provides supporting data for the interaction between Cavin4b and Bin1b and the contribution of Cavin4b to tubule formation. Video 1 shows 3D reconstruction of T-tubule area from *cavin4*$^{-/-}$ muscle. Table S1 provides a list of DNA constructs used in this study. Table S2 provides a list of primers used for qRT-PCR in this study. Data S1 contains the full code for generating region of interest in Fiji (ImageJ). Data S2 contains the full code for generating mean gray value in Fiji (ImageJ).

Acknowledgments

The authors are grateful to Emmanuel Boucrot for discussions regarding Bin1, Michael Kozlov and Gonen Golani for discussion and comments on the manuscript, and Dominic Hunter for assistance with cell-free expression constructs.

This work was supported by the National Health and Medical Research Council of Australia (APP1156489 to R.G. Parton; APP1099251 to R.G. Parton and T.E. Hall), National Health and Medical Research Council Emerging Leader Fellowship (1174145 to J Giacomotto), the Australian Research Council (DP200102559 to T.E. Hall and R.G. Parton), Australian Research Council Centre of Excellence in Convergent Bio-Nano Science and Technology (CE140100036 to R.G. Parton), and Australian Research Council Centre of Excellence in Synthetic Biology (CE200100029 to K. Alexandrov). The work was supported in part by CSIRO–Queensland University of Technology Synthetic Biology Alliance. We are also grateful to The University of Queensland Major Equipment and Infrastructure Scheme. Confocal microscopy was performed at the Australian Cancer Research Foundation/Institute for Molecular Bioscience Dynamic Imaging Facility for Cancer Biology, established with funding from the Australian Cancer Research Foundation. The authors acknowledge the use of the Australian Microscopy & Microanalysis Research Facility at the Center for Microscopy and Microanalysis, The University of Queensland. Genome editing was performed by the Queensland Facility for Advanced Genome Editing, Genome Innovation Hub and the Transgenic Animal Service of Queensland, The University of Queensland.

The authors declare no competing financial interests.

Author contributions: H.P. Lo, T.E. Hall, and R.G. Parton contributed to conceptualization, supervision, visualization, and writing; T.E. Hall and R.G. Parton contributed to funding acquisition; H.P. Lo, Y. Lim, Z. Xiong, N. Martel, S.J. Nixon, and T.E. Hall contributed to investigation, methodology, and formal analysis (zebrafish and mouse experiments); H.P. Lo, Z. Xiong, and M. Bastiani contributed to investigation, methodology, and formal analysis (cell culture experiments); C. Ferguson, N. Ariotti, J. Rae, M. Floetenmeyer, and R.G. Parton contributed to investigation, formal analysis, and visualization (electron microscopy); D. Xia and N.J. Palpant contributed to methodology (mouse and cell CRISPR generation); S.V. Moradi, H. Wang, S. Rahnama, W.A. Johnston, and K. Alexandrov contributed to investigation and formal analysis (cell-free expression and ALPHALisa experiments); Y. Gao, V.A. Tillu, and B.M. Collins contributed to investigation, formal analysis, and visualization (ITC experiments); R.D. Day contributed to methodology (swim tunnel); J. Giacomotto contributed to methodology, investigation, and formal analysis (zebrafish viewpoint experiments); and K.A. Smith contributed to methodology (zebrafish).

Submitted: 9 May 2019
Revised: 2 June 2021
Accepted: 20 September 2021

References

Ariotti, N., T.E. Hall, J. Rae, C. Ferguson, K.A. McMahon, N. Martel, R.E. Webb, R.I. Webb, R.D. Teasdale, and R.G. Parton. 2015. Modular Detection of GFP-Labeled Proteins for Rapid Screening by Electron Microscopy in Cells and Organisms. *Dev. Cell.* 35:513–525. https://doi.org/10.1016/j.devcel.2015.10.016

Ariotti, N., J. Rae, N. Giles, N. Martel, E. Sierecki, Y. Gambin, T.E. Hall, and R.G. Parton. 2018. Ultrastructural localisation of protein interactions using conditionally stable nanobodies. *PLoS Biol.* 16:e2005473. https://doi.org/10.1371/journal.pbio.2005473

Balijepalli, R.C., and T.J. Kamp. 2008. Caveolae, ion channels and cardiac arrhythmias. *Prog. Biophys. Mol. Biol.* 98:149–160. https://doi.org/10.1016/j.pbiomolbio.2009.01.012

Bastiani, M., L. Liu, M.M. Hill, M.P. Jedrychowski, S.J. Nixon, H.P. Lo, D. Abankwa, R. Luetterforst, M. Fernandez-Rojo, M.R. Breen, et al. 2009. MURC/Cavin-4 and cavin family members form tissue-specific caveolar complexes. *J. Cell Biol.* 185:1259–1273. https://doi.org/10.1083/jcb.200903053

Berger, J., and P.D. Currie. 2012. Zebrafish models flex their muscles to shed light on muscular dystrophies. *Dis. Model. Mech.* 5:726–732. https://doi.org/10.1242/dmm.010082

Berger, J., T. Sztal, and P.D. Currie. 2012. Quantification of birefringence readily measures the level of muscle damage in zebrafish. *Biochem. Biophys. Res. Commun.* 423:785–788. https://doi.org/10.1016/j.bbrc.2012.06.040

Butler, M.H., C. David, G.C. Ochoa, Z. Freyberg, L. Daniell, D. Grabs, O. Cremona, and P. De Camilli. 1997. Amphiphysin II (SH3P9; BIN1), a member of the amphiphysin/Rvs family, is concentrated in the cortical cytomatrix of axon initial segments and nodes of ranvier in brain and around T tubules in skeletal muscle. *J. Cell Biol.* 137:1355–1367. https://doi.org/10.1083/jcb.137.6.1355

Carozzi, A.J., E. Ikonen, M.R. Lindsay, and R.G. Parton. 2000. Role of cholesterol in developing T-tubules: analogous mechanisms for T-tubule and caveolae biogenesis. *Traffic.* 1:326–341. https://doi.org/10.1034/j.1600-0854.2000.010406.x

Cheng, J.P., C. Mendoza-Topaz, G. Howard, J. Chadwick, E. Shvets, A.S. Cowburn, B.J. Dunmore, A. Crosby, N.W. Morrell, and B.J. Nichols. 2015. Caveolae protect endothelial cells from membrane rupture during increased cardiac output. *J. Cell Biol.* 211:53–61. https://doi.org/10.1083/jcb.201504042

Concordet, J.P., and M. Haeussler. 2018. CRISPOR: intuitive guide selection for CRISPR/Cas9 genome editing experiments and screens. *Nucleic Acids Res.* 46(W1):W242–W245. https://doi.org/10.1093/nar/gky354

Cowling, B.S., I. Prokic, H. Tasfaout, A. Rabai, F. Humbert, B. Rinaldi, A.S. Nicot, C. Kretz, S. Friant, A. Roux, and J. Laporte. 2017. Amphiphysin (BIN1) negatively regulates dynamin 2 for normal muscle maturation. *J. Clin. Invest.* 127:4477–4487. https://doi.org/10.1172/JCI90542

Don, E.K., I. Formella, A.P. Badrock, T.E. Hall, M. Morsch, E. Hortle, A. Hogan, S. Chow, S.S. Gwee, J.J. Stoddart, et al. 2017. A Tol2 Gateway-Compatible Toolbox for the Study of the Nervous System and Neurodegenerative Disease. *Zebrafish.* 14:69–72. https://doi.org/10.1089/zeb.2016.1321

Drab, M., P. Verkade, M. Elger, M. Kasper, M. Lohn, B. Lauterbach, J. Menne, C. Lindschau, F. Mende, F.C. Luft, et al. 2001. Loss of caveolae, vascular dysfunction, and pulmonary defects in caveolin-1 gene-disrupted mice. *Science.* 293:2449–2452. https://doi.org/10.1126/science.1062688

Dulhunty, A.F., and C. Franzini-Armstrong. 1975. The relative contributions of the folds and caveolae to the surface membrane of frog skeletal muscle fibres at different sarcomere lengths. *J. Physiol.* 250:513–539. https://doi.org/10.1113/jphysiol.1975.sp011068

Flucher, B.E. 1992. Structural analysis of muscle development: transverse tubules, sarcoplasmic reticulum, and the triad. *Dev. Biol.* 154:245–260. https://doi.org/10.1016/0012-1606(92)90065-O

Fra, A.M., E. Williamson, K. Simons, and R.G. Parton. 1995. De novo formation of caveolae in lymphocytes by expression of VIP21-caveolin. *Proc. Natl. Acad. Sci. USA.* 92:8655–8659. https://doi.org/10.1073/pnas.92.19.8655

Franzini-Armstrong, C. 1991. Simultaneous maturation of transverse tubules and sarcoplasmic reticulum during muscle differentiation in the mouse. *Dev. Biol.* 146:353–363. https://doi.org/10.1016/0012-1606(91)90237-W

Franzini-Armstrong, C. 2018. The relationship between form and function throughout the history of excitation-contraction coupling. *J. Gen. Physiol.* 150:189–210. https://doi.org/10.1085/jgp.201711889

Franzini-Armstrong, C., L. Landmesser, and G. Pilar. 1975. Size and shape of transverse tubule openings in frog twitch muscle fibers. *J. Cell Biol.* 64: 493–497. https://doi.org/10.1083/jcb.64.2.493

Gagnon, J.A., E. Valen, S.B. Thyme, P. Huang, L. Akhmetova, A. Pauli, T.G. Montague, S. Zimmerman, C. Richter, and A.F. Schier. 2014. Efficient mutagenesis by Cas9 protein-mediated oligonucleotide insertion and large-scale assessment of single-guide RNAs. *PLoS One.* 9:e98186. https://doi.org/10.1371/journal.pone.0098186

Galbiati, F., J.A. Engelman, D. Volonte, X.L. Zhang, C. Minetti, M. Li, H. Hou Jr., B. Kneitz, W. Edelmann, and M.P. Lisanti. 2001. Caveolin-3 null mice show a loss of caveolae, changes in the microdomain distribution of the dystrophin-glycoprotein complex, and t-tubule abnormalities. *J. Biol. Chem.* 276:21425–21433. https://doi.org/10.1074/jbc.M100828200

Giacomotto, J., S. Rinkwitz, and T.S. Becker. 2015. Effective heritable gene knockdown in zebrafish using synthetic microRNAs. *Nat. Commun.* 6: 7378. https://doi.org/10.1038/ncomms8378

Gormal, R.S., P. Padmanabhan, R. Kasula, A.T. Bademosi, S. Coakley, J. Giacomotto, A. Blum, M. Joensuu, T.P. Wallis, H.P. Lo, et al. 2020. Modular transient nanoclustering of activated β2-adrenergic receptors revealed by single-molecule tracking of conformation-specific nanobodies. *Proc. Natl. Acad. Sci. USA.* 117:30476–30487. https://doi.org/10.1073/pnas.2007443117

Hagiwara, Y., T. Sasaoka, K. Araishi, M. Imamura, H. Yorifuji, I. Nonaka, E. Ozawa, and T. Kikuchi. 2000. Caveolin-3 deficiency causes muscle degeneration in mice. *Hum. Mol. Genet.* 9:3047–3054. https://doi.org/10.1093/hmg/9.20.3047

Hall, T.E., N. Martel, N. Ariotti, Z. Xiong, H.P. Lo, C. Ferguson, J. Rae, Y.W. Lim, and R.G. Parton. 2020. In vivo cell biological screening identifies an endocytic capture mechanism for T-tubule formation. *Nat. Commun.* 11:3711. https://doi.org/10.1038/s41467-020-17486-w

Hansen, C.G., N.A. Bright, G. Howard, and B.J. Nichols. 2009. SDPR induces membrane curvature and functions in the formation of caveolae. *Nat. Cell Biol.* 11:807–814. https://doi.org/10.1038/ncb1887

Hill, M.M., M. Bastiani, R. Luetterforst, M. Kirkham, A. Kirkham, S.J. Nixon, P. Walser, D. Abankwa, V.M. Oorschot, S. Martin, et al. 2008. PTRF-Cavin, a conserved cytoplasmic protein required for caveola formation and function. *Cell.* 132:113–124. https://doi.org/10.1016/j.cell.2007.11.042

Hohendahl, A., A. Roux, and V. Galli. 2016. Structural insights into the centronuclear myopathy-associated functions of BIN1 and dynamin 2. *J. Struct. Biol.* 196:37–47. https://doi.org/10.1016/j.jsb.2016.06.015

Housley, M.P., B. Njaine, F. Ricciardi, O.A. Stone, S. Hölper, M. Krüger, S. Kostin, and D.Y. Stainier. 2016. Cavin4b/Murcb Is Required for Skeletal Muscle Development and Function in Zebrafish. *PLoS Genet.* 12: e1006099. https://doi.org/10.1371/journal.pgen.1006099

Ibrahim, M., J. Gorelik, M.H. Yacoub, and C.M. Terracciano. 2011. The structure and function of cardiac t-tubules in health and disease. *Proc. Biol. Sci.* 278:2714–2723. https://doi.org/10.1098/rspb.2011.0624

Ishikawa, H. 1968. Formation of elaborate networks of T-system tubules in cultured skeletal muscle with special reference to the T-system formation. *J. Cell Biol.* 38:51–66. https://doi.org/10.1083/jcb.38.1.51

Jacoby, A.S., E. Busch-Nentwich, R.J. Bryson-Richardson, T.E. Hall, J. Berger, S. Berger, C. Sonntag, C. Sachs, R. Geisler, D.L. Stemple, and P.D. Currie. 2009. The zebrafish dystrophic mutant softy maintains muscle fibre viability despite basement membrane rupture and muscle detachment. *Development.* 136:3367–3376. https://doi.org/10.1242/dev.034561

Johnston, W.A., S.V. Moradi, and K. Alexandrov. 2019. Adaption of the Leishmania Cell-Free Expression System to High-Throughput Analysis of Protein Interactions. *Methods Mol. Biol.* 2025:403–421. https://doi.org/10.1007/978-1-4939-9624-7_19

Kawakami, K. 2007. Tol2: a versatile gene transfer vector in vertebrates. *Genome Biol.* 8(Suppl 1):S7. https://doi.org/10.1186/gb-2007-8-s1-s7

Keenan, S.R., and P.D. Currie. 2019. The Developmental Phases of Zebrafish Myogenesis. *J. Dev. Biol.* 7:12. https://doi.org/10.3390/jdb7020012

Kirkham, M., S.J. Nixon, M.T. Howes, L. Abi-Rached, D.E. Wakeham, M. Hanzal-Bayer, C. Ferguson, M.M. Hill, M. Fernandez-Rojo, D.A. Brown, et al. 2008. Evolutionary analysis and molecular dissection of caveola biogenesis. *J. Cell Sci.* 121:2075–2086. https://doi.org/10.1242/jcs.024588

Kwan, K.M., E. Fujimoto, C. Grabher, B.D. Mangum, M.E. Hardy, D.S. Campbell, J.M. Parant, H.J. Yost, J.P. Kanki, and C.B. Chien. 2007. The Tol2kit: a multisite gateway-based construction kit for Tol2 transposon transgenesis constructs. *Dev. Dyn.* 236:3088–3099. https://doi.org/10.1002/dvdy.21343

Lau, P., S.J. Nixon, R.G. Parton, and G.E. Muscat. 2004. RORalpha regulates the expression of genes involved in lipid homeostasis in skeletal muscle cells: caveolin-3 and CPT-1 are direct targets of ROR. *J. Biol. Chem.* 279: 36828–36840. https://doi.org/10.1074/jbc.M404927200

Lee, J., and G.W. Schmid-Schönbein. 1995. Biomechanics of skeletal muscle capillaries: hemodynamic resistance, endothelial distensibility, and pseudopod formation. *Ann. Biomed. Eng.* 23:226–246. https://doi.org/10.1007/BF02584425

Lee, E., M. Marcucci, L. Daniell, M. Pypaert, O.A. Weisz, G.C. Ochoa, K. Farsad, M.R. Wenk, and P. De Camilli. 2002. Amphiphysin 2 (Bin1) and T-tubule biogenesis in muscle. *Science.* 297:1193–1196. https://doi.org/10.1126/science.1071362

Levin, K.R., and E. Page. 1980. Quantitative studies on plasmalemmal folds and caveolae of rabbit ventricular myocardial cells. *Circ. Res.* 46: 244–255. https://doi.org/10.1161/01.RES.46.2.244

Lim, Y.W., H.P. Lo, C. Ferguson, N. Martel, J. Giacomotto, G.A. Gomez, A.S. Yap, T.E. Hall, and R.G. Parton. 2017. Caveolae Protect Notochord Cells against Catastrophic Mechanical Failure during Development. *Curr. Biol.* 27:1968–1981.e7. https://doi.org/10.1016/j.cub.2017.05.067

Liu, L., D. Brown, M. McKee, N.K. Lebrasseur, D. Yang, K.H. Albrecht, K. Ravid, and P.F. Pilch. 2008. Deletion of Cavin/PTRF causes global loss of caveolae, dyslipidemia, and glucose intolerance. *Cell Metab.* 8:310–317. https://doi.org/10.1016/j.cmet.2008.07.008

Lo, H.P., S.J. Nixon, T.E. Hall, B.S. Cowling, C. Ferguson, G.P. Morgan, N.L. Schieber, M.A. Fernandez-Rojo, M. Bastiani, M. Floetenmeyer, et al. 2015. The caveolin-cavin system plays a conserved and critical role in mechanoprotection of skeletal muscle. *J. Cell Biol.* 210:833–849. https://doi.org/10.1083/jcb.201501046

Luetterforst, R., E. Stang, N. Zorzi, A. Carozzi, M. Way, and R.G. Parton. 1999. Molecular characterization of caveolin association with the Golgi complex: identification of a cis-Golgi targeting domain in the caveolin molecule. *J. Cell Biol.* 145:1443–1459. https://doi.org/10.1083/jcb.145.7.1443

Mastronarde, D.N. 2005. Automated electron microscope tomography using robust prediction of specimen movements. *J. Struct. Biol.* 152:36–51. https://doi.org/10.1016/j.jsb.2005.07.007

McMahon, K.A., H. Zajicek, W.P. Li, M.J. Peyton, J.D. Minna, V.J. Hernandez, K. Luby-Phelps, and R.G. Anderson. 2009. SRBC/cavin-3 is a caveolin adapter protein that regulates caveolae function. *EMBO J.* 28:1001–1015. https://doi.org/10.1038/emboj.2009.46

Montague, T.G., J.M. Cruz, J.A. Gagnon, G.M. Church, and E. Valen. 2014. CHOPCHOP: a CRISPR/Cas9 and TALEN web tool for genome editing. *Nucleic Acids Res.* 42(Web Server issue, W1):W401-7. https://doi.org/10.1093/nar/gku410

Nguyen, J.V., I. Soto, K.Y. Kim, E.A. Bushong, E. Oglesby, F.J. Valiente-Soriano, Z. Yang, C.H. Davis, J.L. Bedont, J.L. Son, et al. 2011. Myelination transition zone astrocytes are constitutively phagocytic and have synuclein dependent reactivity in glaucoma. *Proc. Natl. Acad. Sci. USA.* 108: 1176–1181. https://doi.org/10.1073/pnas.1013965108

Nixon, S.J., J. Wegner, C. Ferguson, P.F. Méry, J.F. Hancock, P.D. Currie, B. Key, M. Westerfield, and R.G. Parton. 2005. Zebrafish as a model for

caveolin-associated muscle disease; caveolin-3 is required for myofibril organization and muscle cell patterning. *Hum. Mol. Genet.* 14:1727–1743. https://doi.org/10.1093/hmg/ddi179

Noske, A.B., A.J. Costin, G.P. Morgan, and B.J. Marsh. 2008. Expedited approaches to whole cell electron tomography and organelle mark-up in situ in high-pressure frozen pancreatic islets. *J. Struct. Biol.* 161: 298–313. https://doi.org/10.1016/j.jsb.2007.09.015

Ogata, T., T. Ueyama, K. Isodono, M. Tagawa, N. Takehara, T. Kawashima, K. Harada, T. Takahashi, T. Shioi, H. Matsubara, and H. Oh. 2008. MURC, a muscle-restricted coiled-coil protein that modulates the Rho/ROCK pathway, induces cardiac dysfunction and conduction disturbance. *Mol. Cell. Biol.* 28:3424–3436. https://doi.org/10.1128/MCB.02186-07

Ogata, T., D. Naito, N. Nakanishi, Y.K. Hayashi, T. Taniguchi, K. Miyagawa, T. Hamaoka, N. Maruyama, S. Matoba, K. Ikeda, et al. 2014. MURC/Cavin-4 facilitates recruitment of ERK to caveolae and concentric cardiac hypertrophy induced by α1-adrenergic receptors. *Proc. Natl. Acad. Sci. USA.* 111:3811–3816. https://doi.org/10.1073/pnas.1315359111

Parton, R.G. 1994. Ultrastructural localization of gangliosides; GM1 is concentrated in caveolae. *J. Histochem. Cytochem.* 42:155–166. https://doi.org/10.1177/42.2.8288861

Parton, R.G. 2018. Caveolae: Structure, Function, and Relationship to Disease. *Annu. Rev. Cell Dev. Biol.* 34:111–136. https://doi.org/10.1146/annurev-cellbio-100617-062737

Parton, R.G., M. Way, N. Zorzi, and E. Stang. 1997. Caveolin-3 associates with developing T-tubules during muscle differentiation. *J. Cell Biol.* 136: 137–154. https://doi.org/10.1083/jcb.136.1.137

Plaut, I. 2000. Effects of fin size on swimming performance, swimming behaviour and routine activity of zebrafish Danio rerio. *J. Exp. Biol.* 203: 813–820. https://doi.org/10.1242/jeb.203.4.813

Prokic, I., B.S. Cowling, and J. Laporte. 2014. Amphiphysin 2 (BIN1) in physiology and diseases. *J. Mol. Med. (Berl.).* 92:453–463. https://doi.org/10.1007/s00109-014-1138-1

Rae, J., C. Ferguson, N. Ariotti, R.I. Webb, H.H. Cheng, J.L. Mead, J.D. Riches, D.J. Hunter, N. Martel, J. Baltos, et al. 2021. A robust method for particulate detection of a genetic tag for 3D electron microscopy. *eLife.* 10: e64630. https://doi.org/10.7554/eLife.64630

Richter, T., M. Floetenmeyer, C. Ferguson, J. Galea, J. Goh, M.R. Lindsay, G.P. Morgan, B.J. Marsh, and R.G. Parton. 2008. High-resolution 3D quantitative analysis of caveolar ultrastructure and caveola-cytoskeleton interactions. *Traffic.* 9:893–909. https://doi.org/10.1111/j.1600-0854.2008.00733.x

Rodriguez, G., T. Ueyama, T. Ogata, G. Czernuszewicz, Y. Tan, G.W. Dorn II, R. Bogaev, K. Amano, H. Oh, H. Matsubara, et al. 2011. Molecular genetic and functional characterization implicate muscle-restricted coiled-coil gene (MURC) as a causal gene for familial dilated cardiomyopathy. *Circ. Cardiovasc. Genet.* 4:349–358. https://doi.org/10.1161/CIRCGENETICS.111.959866

Savio-Galimberti, E., J. Frank, M. Inoue, J.I. Goldhaber, M.B. Cannell, J.H. Bridge, and F.B. Sachse. 2008. Novel features of the rabbit transverse tubular system revealed by quantitative analysis of three-dimensional reconstructions from confocal images. *Biophys. J.* 95:2053–2062. https://doi.org/10.1529/biophysj.108.130617

Schiaffino, S., M. Cantini, and S. Sartore. 1977. T-system formation in cultured rat skeletal tissue. *Tissue Cell.* 9:437–446. https://doi.org/10.1016/0040-8166(77)90004-0

Seemann, E., M. Sun, S. Krueger, J. Tröger, W. Hou, N. Haag, S. Schüler, M. Westermann, C.A. Huebner, B. Romeike, et al. 2017. Deciphering caveolar functions by *syndapin III* KO-mediated impairment of caveolar invagination. *eLife.* 6:e29854. https://doi.org/10.7554/eLife.29854

Sinha, B., D. Köster, R. Ruez, P. Gonnord, M. Bastiani, D. Abankwa, R.V. Stan, G. Butler-Browne, B. Vedie, L. Johannes, et al. 2011. Cells respond to mechanical stress by rapid disassembly of caveolae. *Cell.* 144:402–413. https://doi.org/10.1016/j.cell.2010.12.031

Smith, K.A., A.K. Lagendijk, A.D. Courtney, H. Chen, S. Paterson, B.M. Hogan, C. Wicking, and J. Bakkers. 2011. Transmembrane protein 2 (Tmem2) is required to regionally restrict atrioventricular canal boundary and endocardial cushion development. *Development.* 138:4193–4198. https://doi.org/10.1242/dev.065375

Smith, L.L., V.A. Gupta, and A.H. Beggs. 2014. Bridging integrator 1 (Bin1) deficiency in zebrafish results in centronuclear myopathy. *Hum. Mol. Genet.* 23:3566–3578. https://doi.org/10.1093/hmg/ddu067

Szabadosova, V., I. Boronova, P. Ferenc, I. Tothova, J. Bernasovska, M. Zigova, J. Kmec, and I. Bernasovsky. 2018. Analysis of selected genes associated with cardiomyopathy by next-generation sequencing. *J. Clin. Lab. Anal.* 32:e22254. https://doi.org/10.1002/jcla.22254

Tagawa, M., T. Ueyama, T. Ogata, N. Takehara, N. Nakajima, K. Isodono, S. Asada, T. Takahashi, H. Matsubara, and H. Oh. 2008. MURC, a muscle-restricted coiled-coil protein, is involved in the regulation of skeletal myogenesis. *Am. J. Physiol. Cell Physiol.* 295:C490–C498. https://doi.org/10.1152/ajpcell.00188.2008

Tang, R., A. Dodd, D. Lai, W.C. McNabb, and D.R. Love. 2007. Validation of zebrafish (Danio rerio) reference genes for quantitative real-time RT-PCR normalization. *Acta Biochim. Biophys. Sin. (Shanghai).* 39:384–390. https://doi.org/10.1111/j.1745-7270.2007.00283.x

Telfer, W.R., A.S. Busta, C.G. Bonnemann, E.L. Feldman, and J.J. Dowling. 2010. Zebrafish models of collagen VI-related myopathies. *Hum. Mol. Genet.* 19:2433–2444. https://doi.org/10.1093/hmg/ddq126

Thisse, C., and B. Thisse. 2008. High-resolution in situ hybridization to whole-mount zebrafish embryos. *Nat. Protoc.* 3:59–69. https://doi.org/10.1038/nprot.2007.514

Tossavainen, H., O. Aitio, M. Hellman, K. Saksela, and P. Permi. 2016. Structural Basis of the High Affinity Interaction between the Alphavirus Nonstructural Protein-3 (nsP3) and the SH3 Domain of Amphiphysin-2. *J. Biol. Chem.* 291:16307–16317. https://doi.org/10.1074/jbc.M116.732412

Varasteh Moradi, S., D. Gagoski, S. Mureev, P. Walden, K.A. McMahon, R.G. Parton, W.A. Johnston, and K. Alexandrov. 2020. Mapping Interactions among Cell-Free Expressed Zika Virus Proteins. *J. Proteome Res.* 19: 1522–1532. https://doi.org/10.1021/acs.jproteome.9b00771

Villefranc, J.A., J. Amigo, and N.D. Lawson. 2007. Gateway compatible vectors for analysis of gene function in the zebrafish. *Dev. Dyn.* 236:3077–3087. https://doi.org/10.1002/dvdy.21354

Wang, J.T., M.C. Kerr, S. Karunaratne, A. Jeanes, A.S. Yap, and R.D. Teasdale. 2010. The SNX-PX-BAR family in macropinocytosis: the regulation of macropinosome formation by SNX-PX-BAR proteins. *PLoS One.* 5: e13763. https://doi.org/10.1371/journal.pone.0013763

Wang, S.C., S.A. Myers, N.A. Eriksson, R.L. Fitzsimmons, and G.E. Muscat. 2011. Nr4a1 siRNA expression attenuates α-MSH regulated gene expression in 3T3-L1 adipocytes. *Mol. Endocrinol.* 25:291–306. https://doi.org/10.1210/me.2010-0231

Way, M., and R.G. Parton. 1995. M-caveolin, a muscle-specific caveolin-related protein. *FEBS Lett.* 376:108–112. https://doi.org/10.1016/0014-5793(95)01256-7

Wienholds, E., F. van Eeden, M. Kosters, J. Mudde, R.H. Plasterk, and E. Cuppen. 2003. Efficient target-selected mutagenesis in zebrafish. *Genome Res.* 13:2700–2707. https://doi.org/10.1101/gr.1725103

Wilkinson, R.N., S. Elworthy, P.W. Ingham, and F.J. van Eeden. 2013. A method for high-throughput PCR-based genotyping of larval zebrafish tail biopsies. *Biotechniques.* 55:314–316. https://doi.org/10.2144/000114116

Williams, R.J., T.E. Hall, V. Glattauer, J. White, P.J. Pasic, A.B. Sorensen, L. Waddington, K.M. McLean, P.D. Currie, and P.G. Hartley. 2011. The in vivo performance of an enzyme-assisted self-assembled peptide/protein hydrogel. *Biomaterials.* 32:5304–5310. https://doi.org/10.1016/j.biomaterials.2011.03.078

Wu, T., and T. Baumgart. 2014. BIN1 membrane curvature sensing and generation show autoinhibition regulated by downstream ligands and PI(4,5)P2. *Biochemistry.* 53:7297–7309. https://doi.org/10.1021/bi501082r

Xiong, Z., H.P. Lo, K.A. McMahon, N. Martel, A. Jones, M.M. Hill, R.G. Parton, and T.E. Hall. 2021. In vivo proteomic mapping through GFP-directed proximity-dependent biotin labelling in zebrafish. *eLife.* 10:e64631. https://doi.org/10.7554/eLife.64631

JCB

Supplemental material

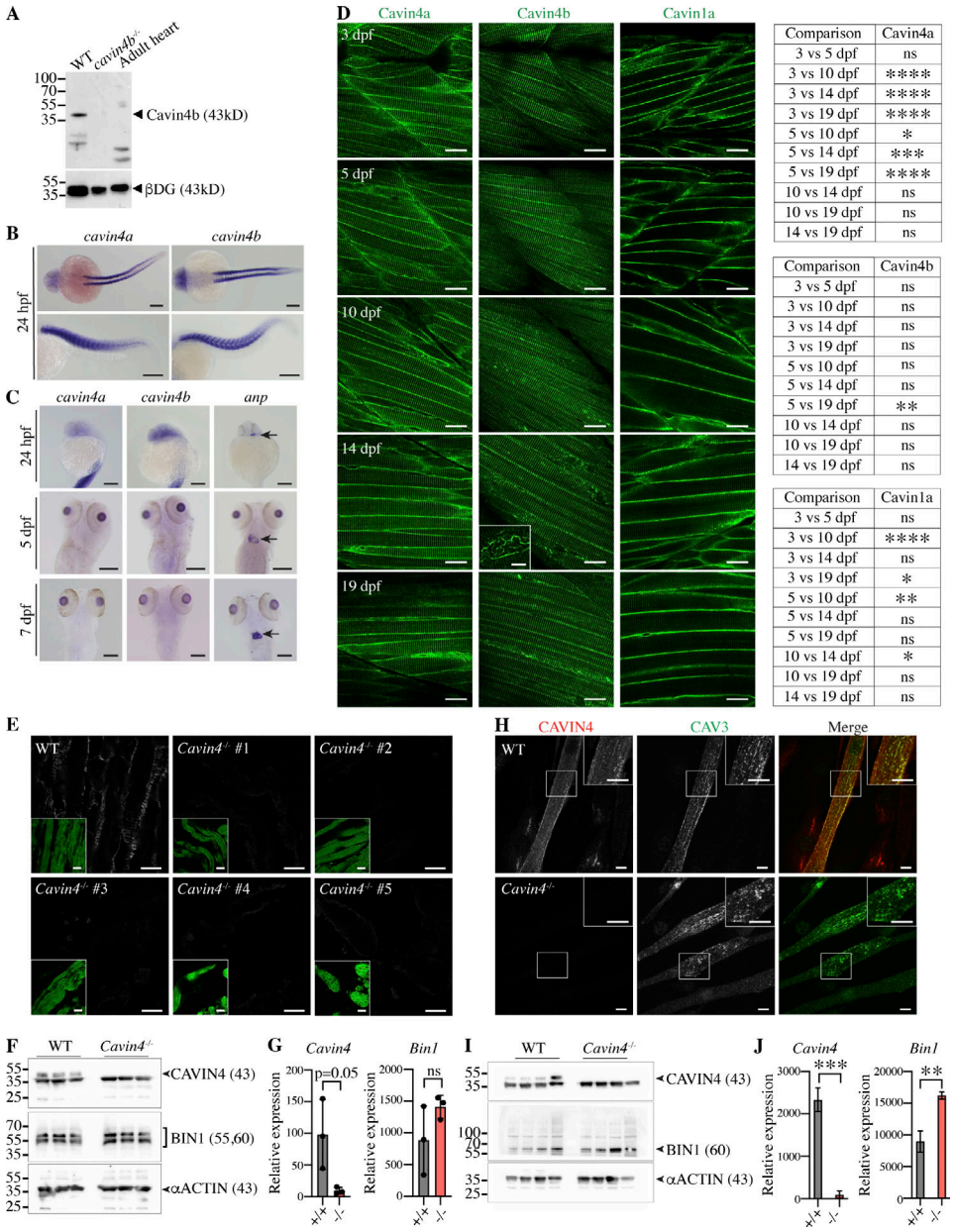

Comparison	Cavin4a
3 vs 5 dpf	ns
3 vs 10 dpf	****
3 vs 14 dpf	****
3 vs 19 dpf	****
5 vs 10 dpf	*
5 vs 14 dpf	***
5 vs 19 dpf	****
10 vs 14 dpf	ns
10 vs 19 dpf	ns
14 vs 19 dpf	ns

Comparison	Cavin4b
3 vs 5 dpf	ns
3 vs 10 dpf	ns
3 vs 14 dpf	ns
3 vs 19 dpf	ns
5 vs 10 dpf	ns
5 vs 14 dpf	ns
5 vs 19 dpf	**
10 vs 14 dpf	ns
10 vs 19 dpf	ns
14 vs 19 dpf	ns

Comparison	Cavin1a
3 vs 5 dpf	ns
3 vs 10 dpf	****
3 vs 14 dpf	ns
3 vs 19 dpf	*
5 vs 10 dpf	**
5 vs 14 dpf	ns
5 vs 19 dpf	ns
10 vs 14 dpf	*
10 vs 19 dpf	ns
14 vs 19 dpf	ns

Figure S1. **Characterization of Cavin4 expression in zebrafish embryos and *Cavin4*$^{-/-}$ mouse muscle and C2C12 myotubes. (A)** Western analysis of Cavin4b expression in 72-hpf WT and *cavin4b*$^{-/-}$ embryos, and adult zebrafish heart tissue. β-Dystroglycan (βDG) is shown as a protein loading control. Image is shown as a merge of chemiluminescent blot and colorimetric image. 15 µg lysate was loaded for each sample. Molecular weight marker (kilodaltons) is shown on left. **(B)** Whole-mount ISH of *cavin4a* and *cavin4b* in 24-hpf WT zebrafish embryos (images anterior to left in both dorsal and lateral view). Note the lack of notochord staining in dorsal view. Scale bars: 200 µm. **(C)** Whole-mount ISH of *cavin4a* and *cavin4b* in 24-hpf, 5-dpf, and 7-dpf WT zebrafish embryos highlighting a lack of *cavin4a* and *cavin4b* expression in the heart (arrows indicate positive control staining of *anp*, a cardiac-specific marker). Scale bars: 200 µm. **(D)** Confocal images showing subcellular localization of Clover-tagged Cavin4a, Cavin4b, and Cavin1a in muscle during zebrafish development (3, 5, 10, 14, and 19 dpf; top to bottom). Scale bars: 20 µm. Subsarcolemmal tubules were occasionally observed in older Cavin4b-Clover fish (inset, 14 dpf; bar: 10 µm). Tables show pairwise comparison of statistical differences observed for T-tubule to sarcolemmal fluorescence intensity ratios over the range of developmental stages (one-way ANOVA with multiple-comparison Tukey's test). *, P ≤ 0.05; **, P ≤ 0.01; ***, P ≤ 0.001; ****, P ≤ 0.0001. **(E)** Confocal images of CAVIN4 (with Phalloidin-Alexa488 counterstain, inset) in 3-d old WT and *Cavin4*$^{-/-}$ mouse skeletal muscle. *Cavin4*$^{-/-}$ *#2* and *#3* were used for analysis shown in Fig. 2. Scale bars: 10 µm. **(F)** Western analysis of CAVIN4 and BIN1 in 3-d old WT and *Cavin4*$^{-/-}$ mouse skeletal muscle (n = 3 each). Total sarcomeric actin (αACTIN) shown as a muscle-specific loading control. 25 µg lysate loaded for each sample. Molecular weight (in parentheses) is in kilodaltons. Molecular weight marker (kilodaltons) is shown on left. **(G)** qRT-PCR of *Cavin4* and *Bin1* expression (relative to *36B4*) in WT (+/+) and *Cavin4*$^{-/-}$ (−/−) mouse skeletal muscle (n = 3 independent samples each for WT and *Cavin4*$^{-/-}$ performed in triplicate, two-tailed t test). **(H)** Confocal images (maximum projection) of CAVIN4 and CAV3 in WT and *Cavin4*$^{-/-}$ C2C12 myotubes. Inset shows boxed areas. Scale bars: 10 µm. **(I)** Western analysis of CAVIN4 and BIN1 in WT and *Cavin4*$^{-/-}$ C2C12 myotubes (n = 4 independent replicates). Total sarcomeric actin (αACTIN) shown as a muscle-specific loading control. 25 µg lysate was loaded for each sample. Molecular weight (in parentheses) is in kilodaltons. Molecular weight marker (kilodaltons) is shown on left. **(J)** qRT-PCR of *Cavin4* and *Bin1* expression (relative to *36B4*) in WT (+/+) and *Cavin4*$^{-/-}$ (−/−) C2C12 myotubes (n = 3 independent samples each of WT and *Cavin4*$^{-/-}$ performed in triplicate, two-tailed t test). **, P ≤ 0.01; ***, P ≤ 0.001. Error bars represent mean ± SD.

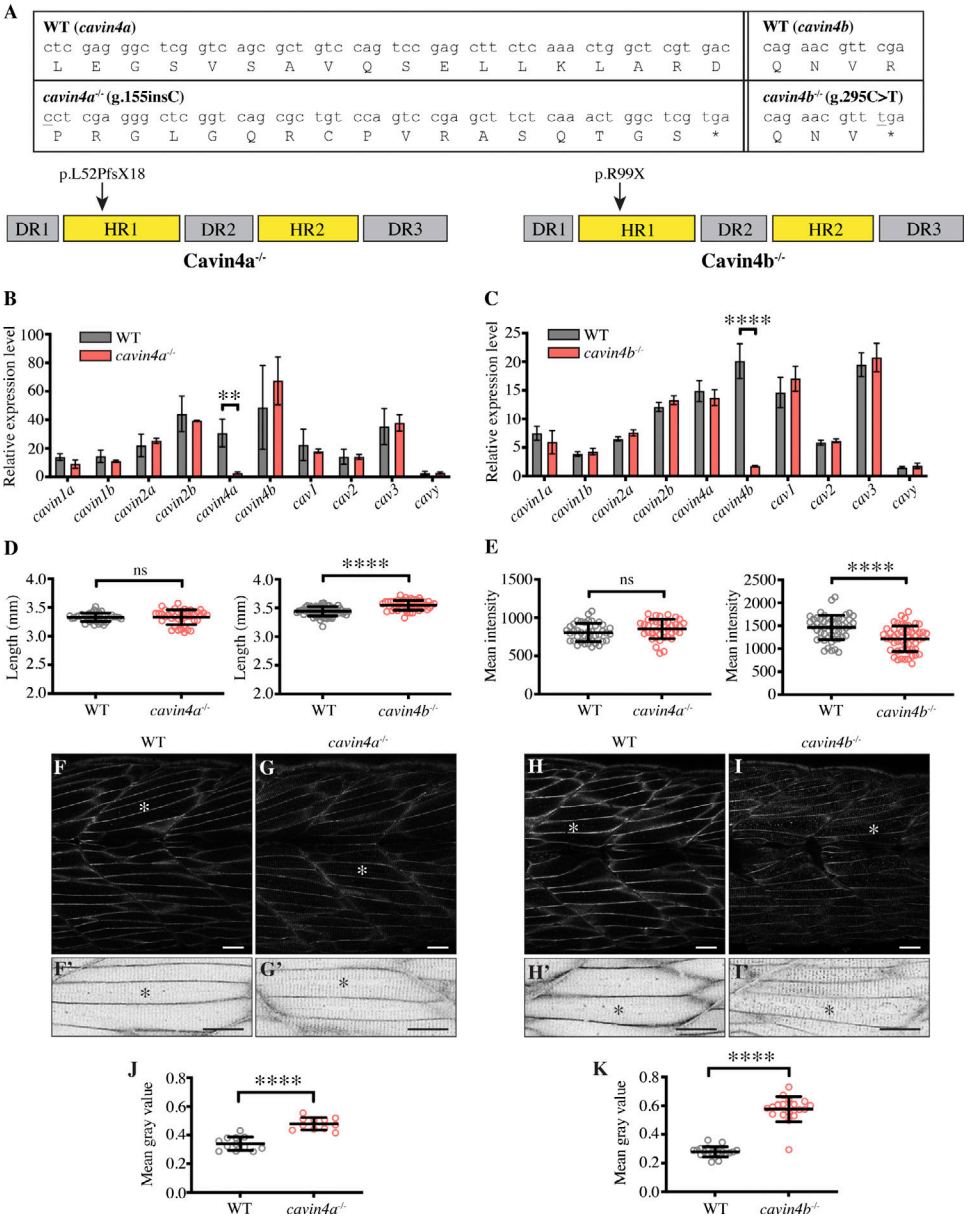

Figure S2. **Generation and characterization of *cavin4a* and *cavin4b* zebrafish mutant lines. (A)** Alignment of nucleotide and amino acid sequences for *cavin4a*^{uq5rp} (*cavin4a*$^{-/-}$) and *cavin4b*^{uq6rp} (*cavin4b*$^{-/-}$) mutant lines in comparison to WT sequences. The CRISPR-generated *cavin4a*$^{-/-}$ line harbors a single base pair insertion (underlined), resulting in a frameshift (truncating stop codon indicated by asterisk) within the helical region 1 (HR1) domain of Cavin4a (arrow). Cavin4a protein domains include DR1 (residues 1–15), DR2 (residues 124–260), and DR3 (residues 270 to C' end) shaded gray; helical regions HR1 (residues 16–123) and helical region 2 (HR2; residues 160–270) shaded yellow. The *cavin4b*$^{-/-}$ line, identified by a TILLING mutagenesis screen, harbors a single point mutation (underlined) resulting in a nonsense mutation within the HR1 domain of Cavin4b (arrow). Cavin4b protein domains: Disordered regions DR1 (residues 1–11), DR2 (residues 120–169) and DR3 (residues 256–319) shaded gray; helical regions HR1 (residues 12–119) and HR2 (residues 170–255) shaded yellow. **(B)** qRT-PCR of caveolae-associated genes (relative to *β-actin*) in WT and *cavin4a*$^{-/-}$ 5-dpf embryos (n = 3 WT clutches and n = 4 *cavin4a*$^{-/-}$ clutches, performed in triplicate, two-tailed t test). **, P ≤ 0.01 for *cavin4a* expression; the remaining comparisons were not significant. **(C)** qRT-PCR of caveolae-associated genes (relative to *β-actin*) in WT and *cavin4b*$^{-/-}$ 5-dpf embryos (n = 4 clutches from each, performed in triplicate, two-tailed t test). ****, P ≤ 0.0001 for *cavin4b* expression; the remaining comparisons were not significant. **(D)** Embryo length (millimeters) for 72-hpf *cavin4a*$^{-/-}$ and *cavin4b*$^{-/-}$ zebrafish embryos in comparison to WT. Quantitation from n = 40 WT and n = 40 *cavin4a*$^{-/-}$ embryos from two clutches, and n = 67 WT and n = 50 *cavin4b*$^{-/-}$ embryos from four and three clutches, respectively (two-tailed t test). Colored circles represent individual embryos. ****, P ≤ 0.0001. **(E)** Mean intensity of birefringence (measured as average gray value of pixels per area) in 5-dpf *cavin4a*$^{-/-}$ and *cavin4b*$^{-/-}$ zebrafish embryos in comparison to WT. Quantitation from n = 40 WT and n = 39 *cavin4a*$^{-/-}$ embryos from two clutches each, and n = 52 WT and n = 52 *cavin4b*$^{-/-}$ embryos from four clutches each (two-tailed t test). Colored circles represent individual embryos. ****, P ≤ 0.0001. **(F–I)** Confocal images of Cav3-EGFP in muscle fibers of live 4-dpf WT (F and H) *cavin4a*$^{-/-}$ (G) and *cavin4b*$^{-/-}$ (I) embryos. Cav3-EGFP–positive embryos were generated from homozygote × heterozygote crosses, and genotyping was performed on embryos after imaging. Area highlighted by the asterisk is magnified in bottom panel (shown as inverted images, F'–I'). Scale bars: 10 µm. **(J and K)** Ratio of T-tubule to sarcolemmal CAV3-EGFP fluorescence intensity in *cavin4a*$^{-/-}$ (J) and *cavin4b*$^{-/-}$ muscle fibers (K) in comparison to WT. Quantitation performed on muscle fibers from n = 12 WT and n = 11 *cavin4a*$^{-/-}$ embryos from two clutches each and from n = 20 WT and n = 19 *cavin4b*$^{-/-}$ embryos from three clutches each (two-tailed t test). Colored circles represent individual embryos. ****, P ≤ 0.0001. Error bars represent mean ± SD.

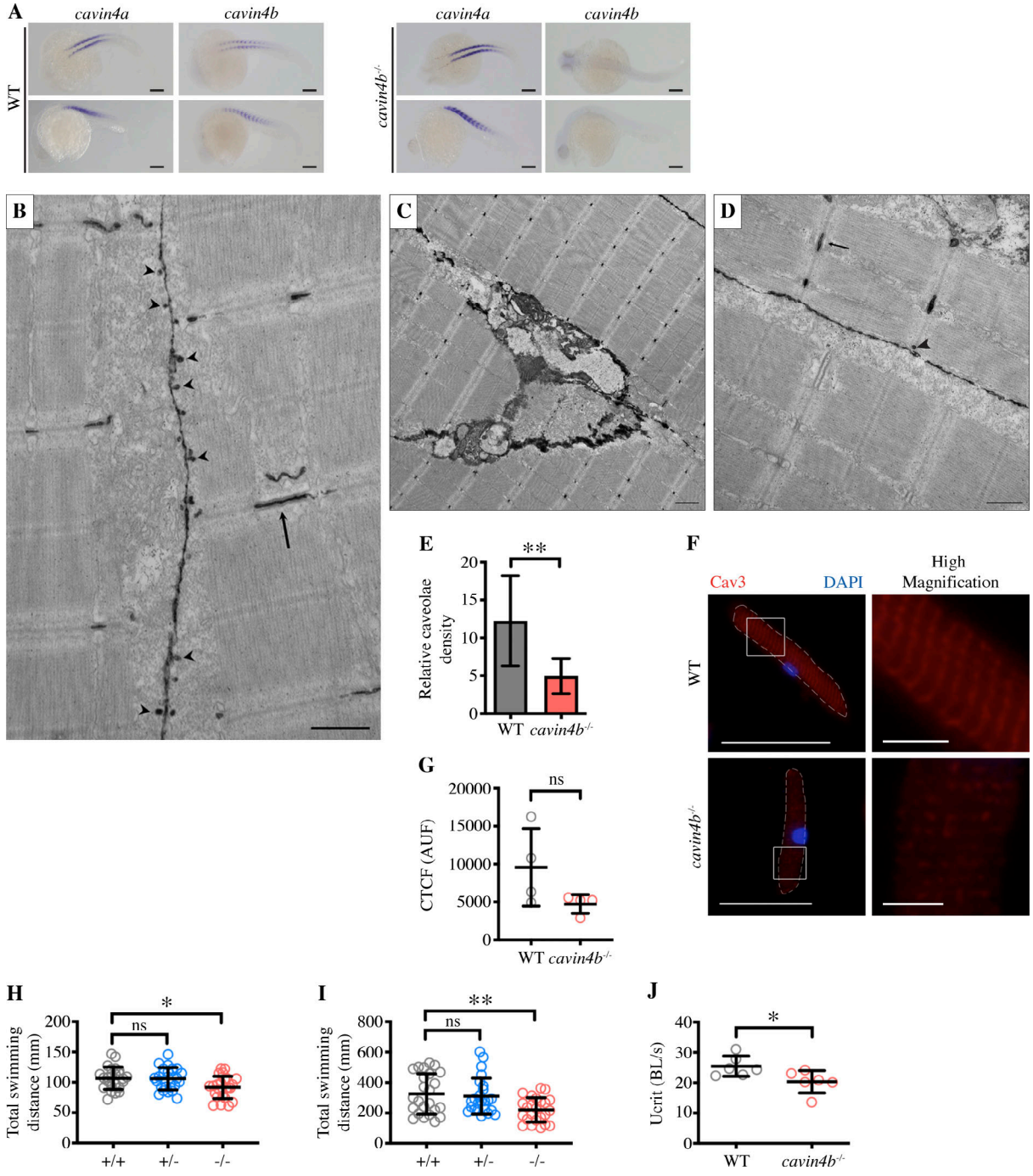

Figure S3. **A loss of Cavin4b leads to reduced caveolae density and impaired swimming ability in zebrafish muscle. (A)** Whole-mount ISH of *cavin4a* and *cavin4b* in WT and *cavin4b*$^{-/-}$ 24-hpf zebrafish embryos, showing loss of *cavin4b* signal in *cavin4b*$^{-/-}$ embryos. Images shown anterior to left in both dorsal and lateral view (upper and lower panel, respectively). Scale bars: 200 µm. **(B–D)** Ultrastructural analysis of 5-dpf WT (B) and *cavin4b*$^{-/-}$ (C-D) zebrafish embryos. Normal sarcomeric structure and T-system (arrows, B and D) was observed in WT and *cavin4b*$^{-/-}$ embryos. An abundance of caveolae was observed in WT muscle (arrowheads, B), but relatively few caveolae were observed in *cavin4b*$^{-/-}$ muscle (arrowhead, D). Scale bars: B and D, 500 nm; C, 1 µm. **(E)** Relative caveolae density was 43.7 ± 15.0% in 5-dpf *cavin4b*$^{-/-}$ muscle in comparison to WT (n = 3 each of WT and *cavin4b*$^{-/-}$ fibers, two-tailed t test). **, P ≤ 0.01. **(F)** Cav3 immunofluorescence (with DAPI counterstain) in isolated muscle fibers from 4-dpf WT and *cavin4b*$^{-/-}$ embryos. Muscle fibers are highlighted with a dashed line. Images in right panel represent higher magnification of boxed areas. Scale bars: 30 µm (left panel); 5 µm (right panel). **(G)** CTCF of Cav3 in 4-dpf WT and *cavin4b*$^{-/-}$ muscle fibers (n = 86 fibers from 4 WT clutches and n = 65 fibers from 4 *cavin4b*$^{-/-}$ clutches, two-tailed t test). CTCF values (AUF, arbitrary unit of fluorescence) were calculated by subtracting mean fluorescence of background signal from the integrated density of a whole muscle fiber. Colored circles represent the four independent clutches. **(H and I)** 7-dpf WT (+/+), *cavin4b*$^{+/-}$ (+/–), and *cavin4b*$^{-/-}$ (–/–) zebrafish embryos were placed in a 24-well plate, and total swimming distance (millimeters) over 10 min under light was recorded (one-way ANOVA with multiple-comparison Dunnett's test). H and I represent two independent experiments. *Cavin4b*$^{+/-}$ embryos were generated from WT × *cavin4b*$^{-/-}$ crosses. Colored circles represent individual embryos (n = 24 each). *, P ≤ 0.05; **, P ≤ 0.01. **(J)** Critical swimming speed (Ucrit) measured as body lengths per second (BL/s) in WT and *cavin4b*$^{-/-}$ adult zebrafish. Colored circles represent individual fish (n = 6 each, two-tailed t test). *, P ≤ 0.05. Error bars represent mean ± SD.

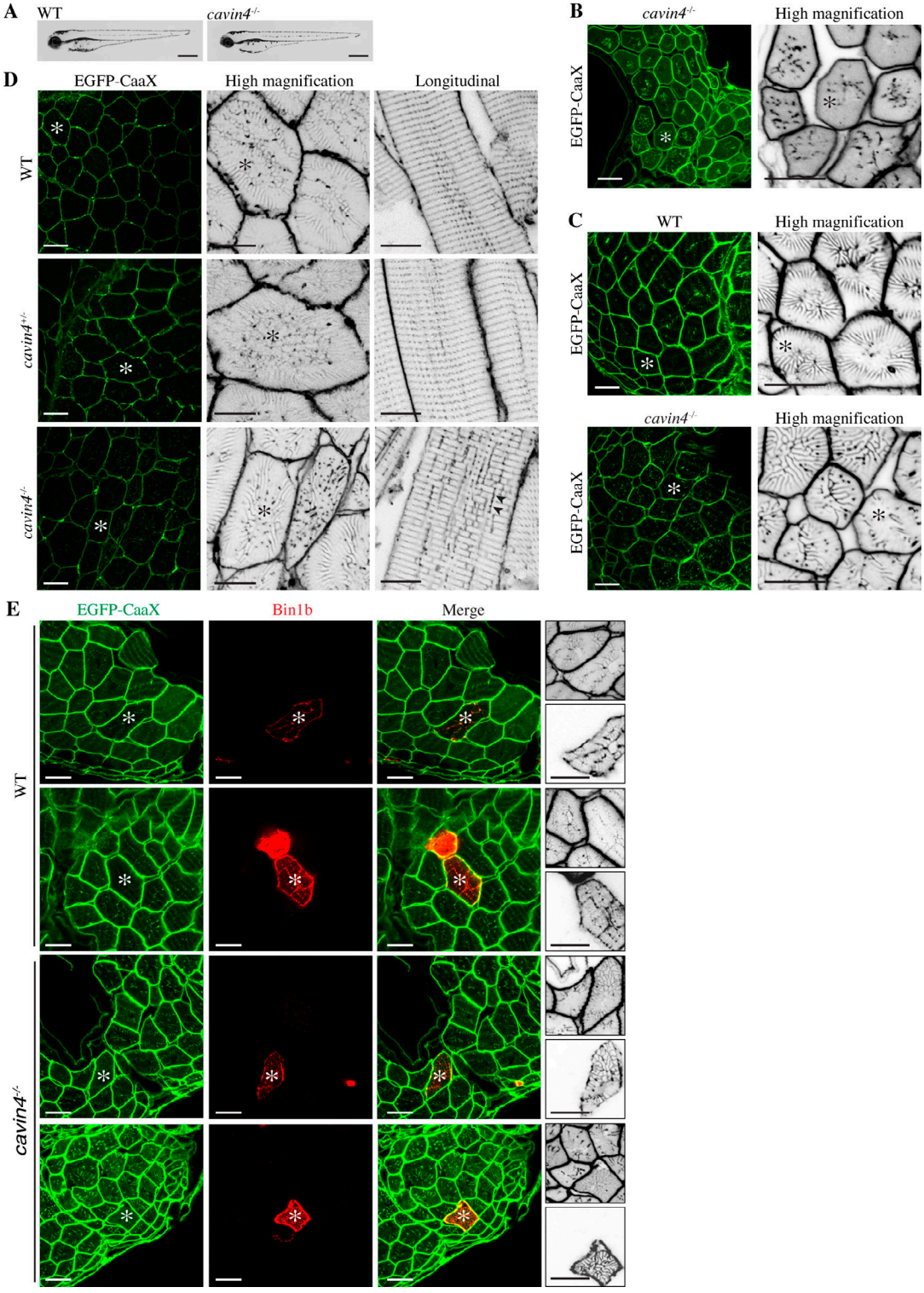

Figure S4. **T-tubule dysmorphology in *cavin4*$^{-/-}$ zebrafish muscle is ameliorated by high expression of Bin1b. (A)** General morphology of *cavin4*$^{-/-}$ zebrafish embryo at 72 hpf in comparison to a WT embryo. Scale bars: 500 µm. **(B)** Confocal image of a more severe EGFP-CaaX localization pattern in a transverse section of a 5-dpf *cavin4*$^{-/-}$ embryo. Asterisk indicates corresponding muscle fiber in higher magnification (shown as an inverted image) on right. Scale bars: 10 µm. **(C)** Confocal images of EGFP-CaaX in transverse sections of 10-dpf WT and *cavin4*$^{-/-}$ embryos. Asterisk indicates corresponding muscle fiber in higher magnification (shown as an inverted image) on right. Scale bars: 10 µm. **(D)** Confocal images of EGFP-CaaX in transverse sections of 30-dpf WT, *cavin4*$^{+/-}$, and *cavin4*$^{-/-}$ embryos (bars: 20 µm). Asterisk indicates corresponding muscle fiber in higher magnification (shown as an inverted image) in the middle panel (bars: 10 µm). Images of muscle fibers in longitudinal orientation are shown as inverted images in far right panel; arrowheads indicate longitudinal tubules (scale bars: 10 µm). *Cavin4*$^{+/-}$ embryos are clutchmates of *cavin4*$^{-/-}$ embryos. **(E)** Confocal images of EGFP-CaaX in transverse sections of WT and *cavin4*$^{-/-}$ muscle fibers with transient overexpression of mKate2-Bin1b. Asterisks indicate corresponding muscle fibers; smaller panels on the far right (shown as inverted images) represent higher magnification of these fibers (top image: EGFP-CaaX; bottom image: mKate2-Bin1b). Scale bars: 10 µm.

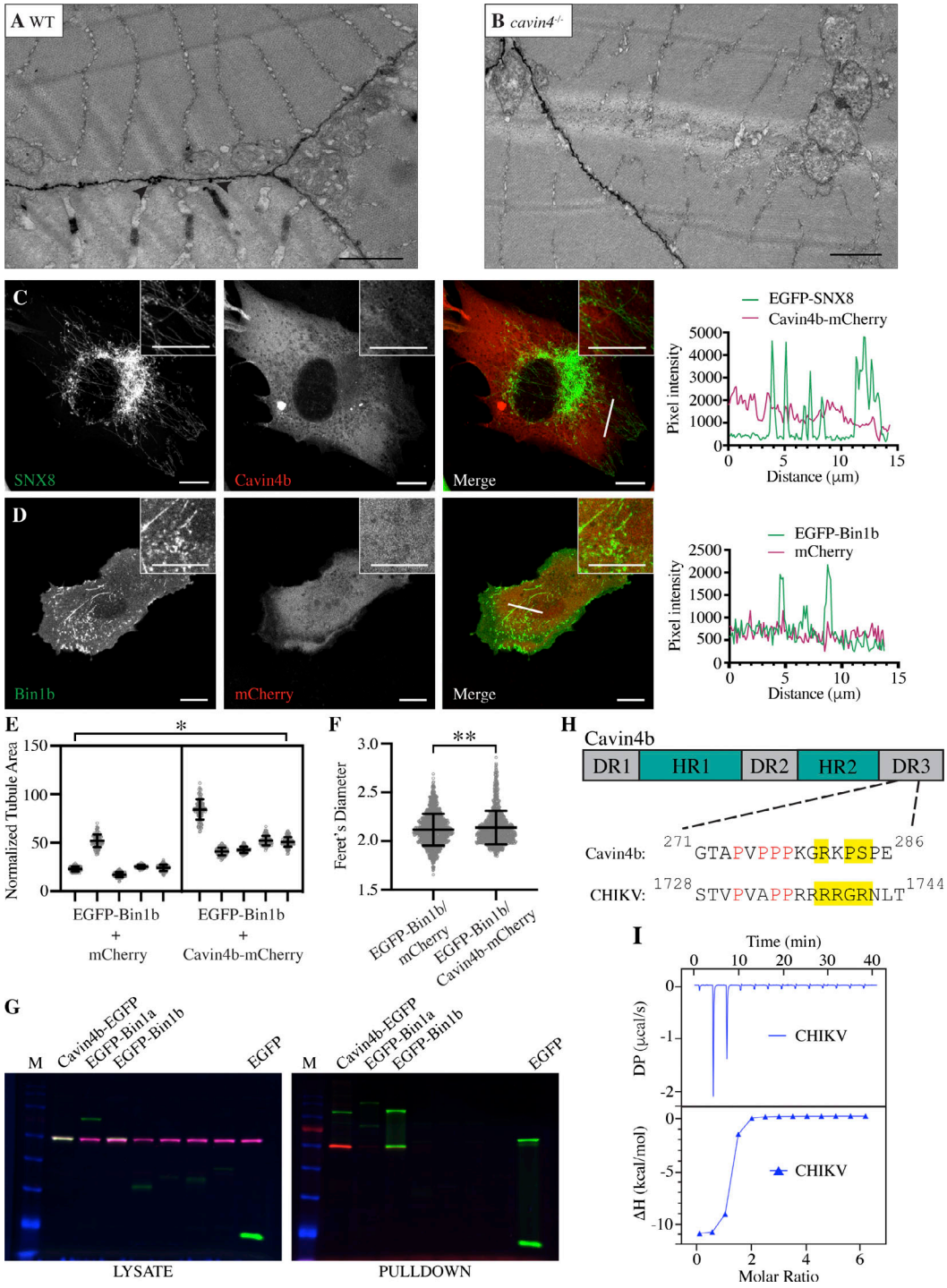

Figure S5. **An interaction between Bin1b and Cavin4b contributes to tubule formation. (A and B)** Ultrastructural analysis of 5-dpf WT (A) and *cavin4*$^{-/-}$ (B) zebrafish embryos. Arrowheads indicate caveolae in WT embryo. Scale bars: 1 µm. **(C and D)** Live confocal imaging of BHK cells cotransfected with: EGFP-SNX8/Cavin4b-mCherry (C, *n* = 5 cells imaged) or EGFP-Bin1b/mCherry (D, *n* = 3 cells imaged each in five independent experiments). Colocalization was analyzed by line scan (as indicated; inset shows line scan area) showing pixel intensity over the line distance (far right panel). Scale bars: 10 µm. **(E and F)** Scatter plot quantitation of tubule area (E) and average Feret's diameter (F) of Bin1b-positive tubules in the presence of Cavin4b-mCherry or mCherry reporter during time-lapse imaging over 6 min (*n* = 5 cells analyzed). Tubule area was normalized to cell size. For E, nested two-tailed *t* test, area normalized to cell size. For F, two-tailed *t* test. *, P ≤ 0.05; **, P ≤ 0.01. Error bars represent mean ± SD. **(G)** Uncropped gels from Fig. 6 B (shown as a multichannel image). Pull-down using GFPtrap with a maltose binding protein tag with in-gel fluorescence detection after semi-denaturing PAGE. Cavin4b-mCherry was coexpressed with Cavin4b-EGFP (positive control), EGFP-Bin1a, EGFP-Bin1b, or EGFP (reporter only negative control) in BHK cells. Protein in starting lysate is shown on left, pull-down using GFPtrap with a maltose binding protein tag is shown on right. Proteins in pull-down fraction appear as a doublet due to binding to maltose. M, molecular weight marker. **(H)** Schematic of zebrafish Cavin4b protein domains (HR, helical region). Alignment between PRD within DR3 of Cavin4b and the SH3-binding region of CHIKV is shown; proline residues are in red, and positively charged amino acids are highlighted in yellow. **(I)** Direct association of Bin1b SH3 domain with CHIKV peptide as measured by ITC.

Video 1. **3D reconstruction of T-tubule area from *cavin4*$^{-/-}$ muscle (related to Fig. 4 N).** Frame rate is 8 frames per second.

Two tables and two datasets are provided online. Table S1 lists DNA constructs used in this study. Table S2 lists qRT-PCR primers used in this study. Data S1 contains the full code for generating region of interest in Fiji (ImageJ). Data S2 contains the full code for generating mean gray value in Fiji (ImageJ).